

DETERMINING THE COSMIC DISTANCE SCALE FROM INTERFEROMETRIC
MEASUREMENTS OF THE SUNYAEV-ZEL'DOVICH EFFECT

ERIK D. REESE^{1,2,3}, JOHN E. CARLSTROM¹, MARSHALL JOY⁴, JOSEPH J. MOHR⁵, LAURA GREGO⁶,
WILLIAM L. HOLZAPFEL²
Draft version November 6, 2018

ABSTRACT

We determine the distances to 18 galaxy clusters with redshifts ranging from $z \sim 0.14$ to $z \sim 0.78$ from a maximum likelihood joint analysis of 30 GHz interferometric Sunyaev-Zel'dovich effect (SZE) and X-ray observations. We model the intracluster medium (ICM) using a spherical isothermal β model. We quantify the statistical and systematic uncertainties inherent to these direct distance measurements, and we determine constraints on the Hubble parameter for three different cosmologies. These distances imply a Hubble constant of $60^{+4}_{-4} \text{ } ^{+13}_{-18} \text{ km s}^{-1} \text{ Mpc}^{-1}$ for an $\Omega_M = 0.3$, $\Omega_\Lambda = 0.7$ cosmology, where the uncertainties correspond to statistical followed by systematic at 68% confidence. With a sample of 18 clusters, systematic uncertainties clearly dominate. The systematics are observationally approachable and will be addressed in the coming years through the current generation of X-ray satellites (Chandra & XMM-Newton) and radio observatories (OVRO, BIMA, & VLA). Analysis of high redshift clusters detected in future SZE and X-ray surveys will allow a determination of the geometry of the universe from SZE determined distances.

Subject headings: cosmic microwave background — cosmology: observations — distance scale — galaxies: clusters — techniques: interferometric

1. INTRODUCTION

Analysis of Sunyaev-Zel'dovich effect (SZE) and X-ray data provides a method of directly determining distances to galaxy clusters at any redshift. Clusters of galaxies contain hot ($k_B T_e \sim 10$ keV) gas, known as the intracluster medium (ICM), trapped in their potential wells. Cosmic microwave background (CMB) photons passing through a massive cluster interact with the energetic ICM electrons with a $\tau \approx 0.01$ probability. This inverse Compton scattering preferentially boosts the energy of a scattered CMB photon causing a small ($\lesssim 1$ mK) distortion in the CMB spectrum, known as the Sunyaev-Zel'dovich effect (Sunyaev & Zel'dovich 1970, 1972). The SZE appears as a decrement for frequencies $\lesssim 218$ GHz and as an increment for frequencies $\gtrsim 218$ GHz. The SZE is proportional to the pressure integrated along the line of sight $\Delta T \propto \int n_e T_e dl$. X-ray emission from the ICM has a different dependence on the density $S_x \propto \int n_e^2 \Lambda_{eH} dl$, where Λ_{eH} is the X-ray cooling function. Taking advantage of the different density dependencies and with some assumptions about the geometry of the cluster, the distance to the cluster may be determined. SZE and X-ray determined distances are independent of the extragalactic distance ladder and provide distances to high redshift galaxy clusters. The promise of direct distances has been one of the primary motivations for SZE observations.

In the last decade, SZE detections have become routine due to advances in both instrumentation and observational strategy. Recent high signal-to-noise ratio detections have been made with single dish observations at radio wavelengths (Birkinshaw & Hughes 1994; Herbig et al. 1995; Myers et al. 1997; Hughes & Birkinshaw 1998), millimeter wavelengths (Holzapfel et al. 1997a,b; Pointecouteau et al. 1999, 2001) and submillimeter wavelengths (Lamarre et al. 1998; Komatsu et al. 1999). Interferometric observations at centimeter wavelengths are now routinely producing high quality images of the SZE (Jones et al. 1993; Grainge et al. 1993; Carlstrom et al. 1996; Carlstrom et al. 1998; Saunders et al. 1999; Grainge et al. 2002b; Reese et al. 2000; Grego et al. 2000; Carlstrom et al. 2000; Grego et al. 2001; Jones et al. 2002).

In this paper, we present a maximum likelihood joint analysis of our 30 GHz interferometric SZE observations with archival *Röntgen Satellite* (ROSAT) X-ray imaging observations. Cluster X-ray temperatures, metallicity, and H I column densities are taken from the literature. The intracluster medium (ICM) is modeled as a spherical isothermal β model. We refine the analysis technique described in Reese et al. (2000) and apply it to a sample of 18 clusters for which we determine distances. These distances are then used to measure the Hubble constant. This is the largest homogeneously analyzed sample of SZE clusters with distance determinations thus far. To date, there are about 20 published estimates of H_0 based on combining X-ray and SZE data for individual clusters (see Birkinshaw 1999, for a review and compiled distances). Most notably, those results include one sample consisting of 7 nearby ($z < 0.1$) galaxy clusters (Mason et al. 2001; Mason 1999; Myers et al. 1997) and a sample of 5 intermediate redshift ($0.14 < z < 0.3$) clusters (Jones et al. 2002).

The cluster sample selection for this paper is discussed in §2. The centimeter wave SZE system and interferometric SZE data are described in §3.1. A brief overview the ROSAT X-ray cluster data is given in §3.2. The analysis method,

¹ Department of Astronomy & Astrophysics, University of Chicago, 5640 S. Ellis Ave., Chicago, IL 60637

² Department of Physics, University of California, Berkeley, CA 94720

³ Chandra Fellow

⁴ Space Science Laboratory, SD50, NASA Marshall Space Flight Center, Huntsville, AL 35812

⁵ Department of Astronomy and Department of Physics, University of Illinois, Urbana, IL 61801

⁶ Harvard-Smithsonian Center for Astrophysics, 60 Garden St., Cambridge, MA 02138

including uncertainty estimation, is outlined in §4 along with the model fitting results. Distances and our determination of the Hubble parameter appear in §5. Sources of possible systematic uncertainties are discussed in §6. Section 7 contains a discussion of the results and future prospects. Throughout this work, the galaxy cluster Cl 0016 + 16 ($z = 0.546$) will be used as the example cluster to illustrate both the analysis method and general results. All uncertainties are 68.3% confidence unless explicitly stated otherwise.

2. CLUSTER SAMPLE

The determination the Hubble parameter requires a large sample of galaxy clusters free of selection effects. For example, clusters selected by X-ray surface brightness will preferentially include clusters elongated along the line of sight. A spherical analysis will underestimate the line of sight length of the cluster, causing the derived Hubble parameter to be biased low. In theory, selecting by X-ray luminosity, L_x , alleviates the selection bias problem. In practice, this is complicated by the fact that X-ray surveys are surface brightness limited; clusters just at the detection limit that are elongated along the line of sight will be detected while clusters just at the detection limit that are instead extended in the plane of the sky will be missed. Staying well above the detection limit of the survey will alleviate this potential pitfall. Observational considerations for cluster sample selection include the declinations of the clusters, the size (redshift) of the cluster, possible radio point sources in the cluster field, and SZE brightness for which we use L_x as an indicator. The Owens Valley Radio Observatory (OVRO) and Berkeley-Illinois-Maryland Association (BIMA) interferometers have been used to observe known X-ray clusters with $z \gtrsim 0.14$, declination $\gtrsim -15^\circ$, and $L_x \gtrsim 5 \times 10^{44} h_{50}^{-2} \text{ erg s}^{-1}$ (0.3-3.5 keV band for *Einstein* and 0.1-2.4 keV band for *ROSAT*). In addition, short, preliminary observations of many clusters are also performed to investigate possible point sources in the field.

The OVRO/BIMA SZE imaging project initially chose targets from the limited number of known X-ray bright clusters. With the publishing of X-ray cluster surveys, the OVRO/BIMA SZE imaging project chose targets from three X-ray catalogs of galaxy clusters: the *Einstein Observatory* Extended Medium Sensitivity Survey, EMSS (Gioia et al. 1990; Stocke et al. 1991; Gioia & Luppino 1994; Maccacaro et al. 1994); the *ROSAT* X-ray Brightest Abell Clusters, XBACs (Ebeling et al. 1996b,a); and the *ROSAT* Brightest Cluster Sample, BCS (Ebeling et al. 2000a; Crawford et al. 1999; Ebeling et al. 1998, 1997). We have also recently included two more recent *ROSAT* samples of distant massive clusters to our cluster selection database: the Wide Angle *ROSAT* Pointed Survey, WARPS (Fairley et al. 2000; Ebeling et al. 2000b; Jones et al. 1998; Scharf et al. 1997); and the MAssive Cluster Survey, MACS (Ebeling et al. 2001). So far, we have high S/N detections in 21 clusters with redshifts $z > 0.45$.

The distance calculation requires three data sets: SZE, X-ray imaging, and X-ray spectroscopic data. We have obtained high signal-to-noise detections of the SZE in 45 galaxy clusters. The subsample of these clusters that also have high signal-to-noise X-ray imaging data and published electron temperatures contains 18 galaxy clusters. Table 1 summarizes the redshifts and X-ray luminosities for each galaxy cluster in our sample.

3. DATA

Here we briefly describe the SZE and X-ray observations and data reduction. Table 2 summarizes the observation times for both the SZE and *ROSAT* observations of each cluster in our sample. The SZE observation times are the total on-source integration times for the interferometric SZE data used in this analysis. The *ROSAT* observation times are the total livetimes of the pointings used in this analysis.

3.1. Interferometric SZE Data

The extremely low systematics of interferometers make them well suited to study the weak SZE signal. A unique feature of interferometers is their ability to separate the diffuse, negative SZE emission from small scale, positive point source emission through the spatial filtering of the interferometer. Interferometers also provide a well defined angular and spectral filter, which is important in the analysis of the SZE data discussed in §4.

3.1.1. Centimeter-Wave System and Observing Strategy

Over the past several summers, we outfitted the Berkeley-Illinois-Maryland Association (BIMA) millimeter array in Hat Creek, California, and the Owens Valley Radio Observatory (OVRO) millimeter array in Big Pine, California, with centimeter wavelength receivers. Our receivers use cooled (~ 10 K) High Electron Mobility Transistor (HEMT) amplifiers (Pospieszalski et al. 1995) operating over 26-36 GHz with characteristic receiver temperatures of $T_{rx} \sim 11$ -20 K over the 28-30 GHz band used for the observations presented here. When combined with the BIMA or OVRO systems, these receivers obtain typical system temperatures scaled to above the atmosphere of $T_{sys} \sim 35$ -45 K. Most telescopes are placed in a compact configuration to maximize sensitivity on angular scales subtended by distant clusters ($\sim 1'$), but telescopes are always placed at longer baselines for simultaneous detection of point sources. Every half hour we observe a bright quasar, commonly called a phase calibrator, for about two minutes to monitor the system phase and gain. The total integration time for each cluster field is given in Table 2 for both OVRO and BIMA.

An interferometer samples the Fourier transform of the sky brightness distribution multiplied by the primary beam rather than the direct image of the sky. The SZE data files include the positions in the Fourier domain, which depend on the arrangement of the telescopes in the array and the declination of the source, the real and imaginary Fourier components, and a measure of the noise in the real and imaginary components. The Fourier conjugate variables to right

TABLE 1
CLUSTER SAMPLE

cluster	redshift	L_x^a ($10^{44}h_{50}^{-2}$ erg s $^{-1}$)	band (keV)	references- z ; L_x
MS 1137.5 + 6625	0.784	5.4	0.3 – 3.5	D99;GL94
MS 0451.6 – 0305	0.550	20.0	0.3 – 3.5	GL94;GL94
Cl 0016 + 16	0.546	14.6	0.3 – 3.5	DG92;GL94
RX J1347.5 – 1145	0.451	73.0	0.1 – 2.4	S95;S97
Abell 370	0.374	11.7 ^b	0.1 – 2.4	M88;AE99
MS 1358.4 + 6245	0.327	10.6	0.3 – 3.5	GL94;GL94
Abell 1995	0.322	13.4	0.1 – 2.4	P00;B00
Abell 611	0.288	8.6	0.1 – 2.4	C95;B00
Abell 697	0.282	19.2	0.1 – 2.4	C95;B00,E98
Abell 1835	0.252	32.6	0.1 – 2.4	SR99;B00,E98
Abell 2261	0.224	20.6	0.1 – 2.4	C95;B00
Abell 773	0.216	12.1	0.1 – 2.4	SR99;B00,E98
Abell 2163	0.202	37.5	0.1 – 2.4	SR99;E96
Abell 520	0.202	14.5	0.1 – 2.4	GL94;B00,E98
Abell 1689	0.183	20.7	0.1 – 2.4	SR91;E96
Abell 665	0.182	15.7	0.1 – 2.4	SR91;B00
Abell 2218	0.171	8.2	0.1 – 2.4	L92;B00
Abell 1413	0.142	10.9	0.1 – 2.4	SR99;B00,E98

^aComputed for a flat $\Omega_M = 1$ universe.

^bConverted the 2–10 keV flux in AE99 to the 0.1–2.4 keV band (approximate factor of 0.9 determined from cooling function calculation).

REF: AE99-Arnaud & Evrard 1999; B00-Böhringer et al. 2000; C95-Crawford et al. 1995; D99-Donahue et al. 1999; DG92-Dressler & Gunn 1992; E96-Ebeling et al. 1996b; E98-Ebeling et al. 1998; GL94-Gioia & Luppino 1994; L92-Le Borgne et al. 1992; M88-Mellier et al. 1988; P00-Patel et al. 2000; S95-Schindler et al. 1995; S97-Schindler et al. 1997; SR91-Struble & Rood 1991; SR99-Struble & Rood 1999;

ascension and declination are commonly called u and v , respectively, and the Fourier domain is commonly referred to as the u - v plane. The real and imaginary Fourier component pairs as a function of u and v are called visibilities.

The finite size of each telescope dish results in an almost Gaussian response pattern, known as the primary beam. The product of the primary beam and the sky brightness distribution is equivalent to a convolution in the Fourier domain. The primary beams are measured using holography data for both OVRO and BIMA. The main lobe of the primary beams are well fit by a Gaussian with a full width at half maximum (FWHM) of 4'.2 for OVRO and 6'.6 for BIMA at 28.5 GHz. However, we use the measured primary beam profiles for our analysis.

The primary beam sets the field of view. The effective resolution, called the synthesized beam, depends on the sampling of the u - v plane and is therefore a function of the configuration of the telescopes and the declination of the source. The cluster SZE signal is largest on the shortest baselines (largest angular scales). The shortest possible baseline is set by the diameter of the telescopes, D . Thus the system is not sensitive to angular scales larger than about $\lambda/2D$, which is $\sim 2'.8$ for BIMA observations and $\sim 1'.7$ for OVRO observations. The compact configuration used for our observations yields significant SZE signal at these angular scales, but filters out signal on larger angular scales. Because of the spatial filtering by the interferometer, it is necessary to fit models directly to the data in the u - v plane, rather than to the deconvolved image.

Interferometers simultaneously measure both the cluster signal and the point sources in the field. The SZE signal is primarily present in the short baseline data while the response of an interferometer to a point source is independent of the baseline. Therefore, observations with a range of baselines allow us to separate the extended cluster emission from point source emission. We show an example of this after first presenting details of deconvolved 30 GHz images (see Jones et al. 1993; Carlstrom et al. 2000, for additional examples).

3.1.2. Data Reduction

The data are reduced using the MIRIAD (Sault et al. 1995) software package at BIMA and using MMA (Scoville et al. 1993) at OVRO. In both cases, data are excised when one telescope is shadowed by another, when cluster data are not straddled by two phase calibrators, when there are anomalous changes in instrumental response between calibrator observations, or when there is spurious correlation. For absolute flux calibration, we use observations of Mars and adopt the brightness temperature from the Rudy (1987) Mars model. For observations not containing Mars, calibrators in those fields are bootstrapped back to the nearest Mars calibration (see Grego et al. 2001 for more details). The observations of the phase calibrators over each summer give us a summer-long calibration of the gains of the BIMA and OVRO interferometers. They both show very little gain variation, changing by less than 1% over a many-hour track, and the average gains remain stable from day to day. In fact, the gains are stable at the $\sim 1\%$ level over a period of months.

TABLE 2
CLUSTER DATA

cluster	Interferometric SZE Data								<i>ROSAT</i> Data	
	OVRO (hr)				BIMA (hr)				PSPC	HRI
	1994	1995	1996	1998	1996	1997	1998	2000	(ks)	(ks)
MS1137	40	48	99.1
MS0451	30	15.4	45.9
C10016	87	13	29 ^a	8	41.6	70.2
R1347	20.0	...	36.1
A370	33	26	31.9
MS1358	9	7	70	...	22.1	29.2
A1995	58	50	37.6
A611	...	45	12	17.2
A697	...	47	27.8
A1835	27	...	8.5	2.8
A2261	...	40	3	16.1
A773	57	9	5 ^a	...	18	16.5
A2163	25	12	2	10	11	...	11.7	35.8
A520	7	13 ^a	23	20	...	4.7	12.6
A1689	...	26	16	13.5	22.5
A665	38 ^a	24	37.0	98.3
A2218	...	64	6	...	20 ^a	12	42.5	35.5
A1413	11	17	7.5	18.6

^aContains 1996 BIMA data with delay loss problem; data only used to make images and not in the analysis.

3.1.3. Data Visualization: 30 GHz Images

Here we present deconvolved images of our 30 GHz interferometric observations. However, we stress that these images are made to demonstrate the data quality. The model fitting is performed in the Fourier plane, where the noise characteristics of the data and the spatial filtering of the interferometer are well understood. The SZE and X-ray image overlays of Figure 2 show that the region of the cluster sampled by the interferometric SZE observations and the X-ray observations is similar for the clusters in our sample. In addition, the interferometer measures a range of angular scales, which is not apparent from the images in Figure 2. Images showing examples of our SZE data at varying resolutions appear in Carlstrom et al. (1996) for Cl0016 and Carlstrom et al. (2000) for R1347.

Point sources are identified from SZE images created with DIFMAP (Pearson et al. 1994) using only the long baseline data ($\gtrsim 2000 \lambda$) and natural weighting (σ^{-2} weight). Approximate positions and fluxes for each point source are obtained from this image and used as inputs for the model fitting discussed in §4.2. The data are separated by observatory, frequency, and year to allow for temporal and spectral variability of the point source flux. The positions and fluxes of the detected point sources from the model fitting are summarized in Table 3. Also listed are the corresponding 1.4 GHz fluxes for these sources from the NRAO VLA Sky Survey (NVSS) (Condon et al. 1998) and the 5 GHz and 15 GHz fluxes for sources in the three cluster fields surveyed by Moffet & Birkinshaw (1989). The uncertainty in the positions of the point sources is $\sim \pm 3''$ at 68.3% confidence based on model fits of point sources described in §4.2. Figure 1 shows the 30 GHz high resolution ($\geq 2000 \lambda$) maps (color scale) with NVSS 1.4 GHz contours. The color scale wedge above each image shows the range in the map in units of mJy beam $^{-1}$. Contours are multiples of twice the NVSS rms (rms ~ 0.45 mJy beam $^{-1}$). The FWHM of the 30 GHz synthesized beam is shown in the lower left hand corner of each panel and the 45'' FWHM beam of the NVSS survey is shown in the lower right hand corner of each panel. Table 4 summarizes the sensitivity and the FWHM of the synthesized beam of the high resolution maps used to find point sources in each field and shown in Figure 1.

Figure 2 shows the deconvolved SZE image contours overlaid on the X-ray images for each cluster in our sample. Negative contours are shown as solid lines and the contours are multiples of twice the rms of each image. The images for MS0451 and Cl0016 have been published previously (Reese et al. 2000), but we include them here so that the entire sample appears together. We use DIFMAP (Pearson et al. 1994) to produce the naturally weighted SZE images. If any point sources are detected in the cluster field, they are subtracted from the data and a Gaussian taper applied to the visibilities to emphasize brightness variations on cluster scales before the image is deconvolved (CLEANed). The half-power radius of the Gaussian taper applied varies between 1000λ and 2000λ , depending of the observatory and telescope configurations used during the observations. Typically a 1000λ half-power radius taper is applied to BIMA data and a 2000λ half-power radius taper is applied to OVRO data. The full-width at half maximum (FWHM) of the synthesized (restoring) beam is shown in the lower left hand corner of each image. Table 4 summarizes the rms sensitivities and the FWHM's of the synthesized beams of the tapered maps shown in Figure 2, as well as the corresponding statistics for the high resolution ($\geq 2000 \lambda$) images. In addition, Table 4 lists the Rayleigh-Jeans (RJ) brightness sensitivities for each tapered, deconvolved image.

3.1.4. Point Source Identification Using Spatial Filtering

The identification and removal of point sources by taking advantage of the spatial filtering of the interferometer is illustrated in the panels of Figure 3 for the BIMA SZE Cl0016 data. During the maximum likelihood joint analysis (see §4.2), radio point sources identified from this procedure are modeled and fit for directly in the u - v plane. Each panel covers the same angular region, roughly $20'$ on a side, and each panel shows the FWHM of the synthesized beam in the lower left hand corner. Above each image is the color scale mapping showing the flux density of the map in units of mJy beam $^{-1}$. Panel *a* shows the “natural” image, which includes all of the data. There is smooth, extended, negative emission in the center of the map; this is the SZE decrement of Cl0016. There is also a bright spot roughly $2'$ south of the cluster that may be a point source. The large scale symmetric pattern is the synthesized beam of the low resolution data (compare to panel *c*); even when all baselines are considered, the SZE signal dominates. Figure 3*b* shows the high resolution map using data with projected baselines $\geq 2000 \lambda$ only. The point source shows up easily now with the characteristic shape of the synthesized beam for these data. We remove the point source by CLEANing. A Gaussian u - v taper (half-power radius of 1000λ) is then applied to the full data set to emphasize the short baselines, corresponding to the angular scales typical of galaxy clusters, and shown in Figure 3*c*. The cluster is apparent as is the symmetric pattern of the synthesized beam. Deconvolving (CLEANing) the tapered image results in panel *d*, which appeared in Figure 2 overlaid on X-ray data. The contours are multiples of twice the rms of the map.

3.2. ROSAT X-ray Data

We use archival *Röntgen Satellite* (ROSAT) data from both the Position Sensitive Proportional Counter (PSPC) and High-Resolution Imager (HRI) instruments. The live times of the observations we use are listed in Table 2 for both PSPC and HRI observations.

3.2.1. Data Reduction

We use the Snowden Extended Source Analysis Software (ESAS) (Snowden et al. 1994; Snowden 1998) to reduce the data. We use the ESAS software to generate a raw counts image, a noncosmic background image, and an exposure map

TABLE 3
RADIO POINT SOURCES

Field	R.A. ^a (J2000) (h m s)	Dec. ^a (J2000) (d ' ")	$F_{30.0}$ (mJy)	$F_{28.5}$ (mJy)	F_{15}^b (mJy)	F_5^b (mJy)	$F_{1.4}^c$ (mJy)
MS1137
MS0451	04 54 22.1	-03 01 25	$1.41^{+0.26}_{-0.26}$	$1.86^{+0.26}_{-0.26}$	$14.9^{+0.7}_{-0.7}$
Cl0016	00 18 31.1	+16 20 45	...	$9.11^{+1.97}_{-1.97}$	$25.0^{+1.5}_{-1.5}$	$84.5^{+1.1}_{-1.1}$	$269.3^{+8.1}_{-8.1}$
R1347	13 47 30.7	-11 45 09	...	$10.81^{+0.19}_{-0.19}$	$47.6^{+1.9}_{-1.9}$
A370	02 39 55.5	-01 34 06	$0.84^{+0.09}_{-0.09}$	$0.77^{+0.07}_{-0.07}$	$11.7^{+1.1}_{-1.1}$
MS1358	13 59 50.6	+62 31 05	...	$1.61^{+0.17}_{-0.17}$
A1995	14 53 00.5	+58 03 19	$0.58^{+0.05}_{-0.05}$	$0.58^{+0.04}_{-0.04}$	$8.9^{+0.9}_{-0.9}$
A611
A697
A1835	14 01 02.0	+02 52 42	...	$2.76^{+0.14}_{-0.14}$	$41.4^{+1.9}_{-1.9}$
	14 01 00.5	+02 51 53	...	$1.16^{+0.15}_{-0.15}$
A2261	17 22 17.1	+32 09 14	$10.10^{+0.24}_{-0.24}$	$10.80^{+0.24}_{-0.24}$	$24.3^{+1.6}_{-1.6}$
A773
A2163	16 15 43.3	-06 08 40	$1.44^{+0.12}_{-0.12}$	$1.44^{+0.08}_{-0.08}$
A520	04 54 01.1	+02 57 47	...	$7.97^{+0.23}_{-0.23}$	$6.7^{+0.5}_{-0.5}$
	04 54 17.0	+02 55 32	...	$1.01^{+0.10}_{-0.10}$	$15.3^{+1.1}_{-1.1}$
	04 54 20.3	+02 54 56	...	$1.03^{+0.12}_{-0.12}$	$27.8^{+1.6}_{-1.6}$
A1689	13 11 31.6	-01 19 33	$1.33^{+0.10}_{-0.10}$	$1.51^{+0.09}_{-0.09}$	$61.0^{+2.5}_{-2.5}$
	13 11 30.1	-01 20 37	$0.45^{+0.09}_{-0.09}$	$0.42^{+0.09}_{-0.09}$	$10.9^{+0.6}_{-0.6}$
A665	08 31 30.9	+65 52 35	...	$4.83^{+0.28}_{-0.28}$	$12.7^{+0.3}_{-0.3}$	$25.7^{+1.6}_{-1.6}$	$31.1^{+1.3}_{-1.3}$
A2218	16 35 22.1	+66 13 23	$4.29^{+0.21}_{-0.21}$	$4.43^{+0.20}_{-0.20}$	$5.0^{+0.6}_{-0.6}$	$2.8^{+0.2}_{-0.2}$...
	16 35 47.7	+66 14 46	$1.36^{+0.10}_{-0.10}$	$1.59^{+0.11}_{-0.11}$	$2.4^{+0.6}_{-0.6}$	$3.7^{+0.3}_{-0.3}$	$18.0^{+1.8}_{-1.8}$
	16 36 16.0	+66 14 23	$2.41^{+0.29}_{-0.29}$	$3.13^{+0.30}_{-0.30}$	$2.0^{+0.5}_{-0.5}$	$4.2^{+0.1}_{-0.1}$	$13.3^{+0.6}_{-0.6}$
A1413	11 55 08.7	+23 26 17	...	$2.01^{+0.23}_{-0.23}$	$28.8^{+1.3}_{-1.3}$

^aPositions from SZE observations.

^bFrom Moffet & Birkinshaw (1989).

^cFrom Condon et al. (1998).

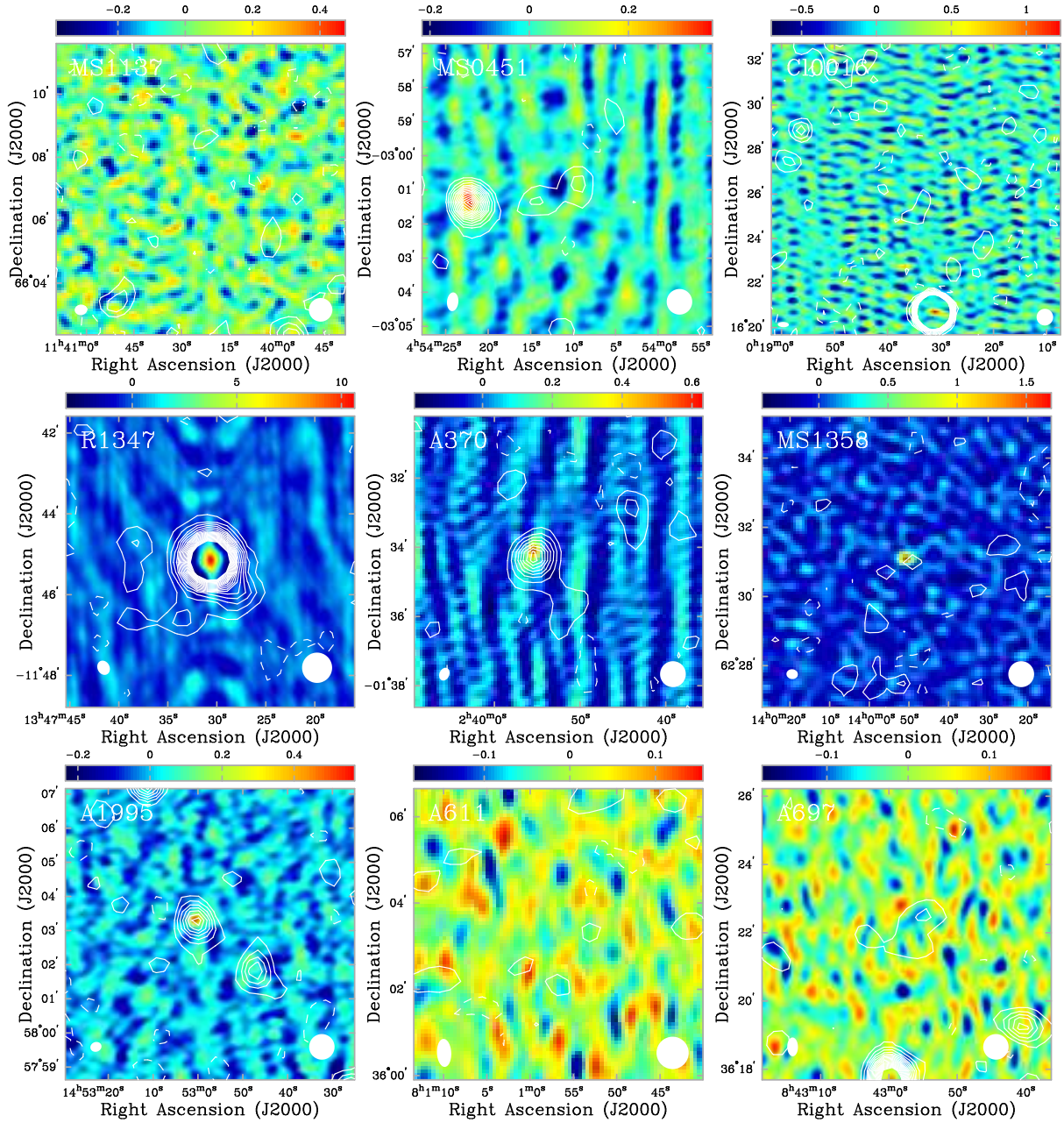


FIG. 1.—High resolution ($\geq 2000 \lambda$) 30 GHz (color scale) with NVSS 1.4 GHz contours. The color scale wedge above each image shows the range in the 30 GHz map in units of mJy beam^{-1} . Contours are multiples of twice the NVSS rms of $\sim 0.45 \text{ mJy beam}^{-1}$. The FWHM of the 30 GHz synthesized beam is shown in the lower left hand corner of each panel and the $45''$ FWHM beam of the NVSS survey is shown in the lower right hand corner of each panel. The 30 GHz image statistics are summarized in Table 4.

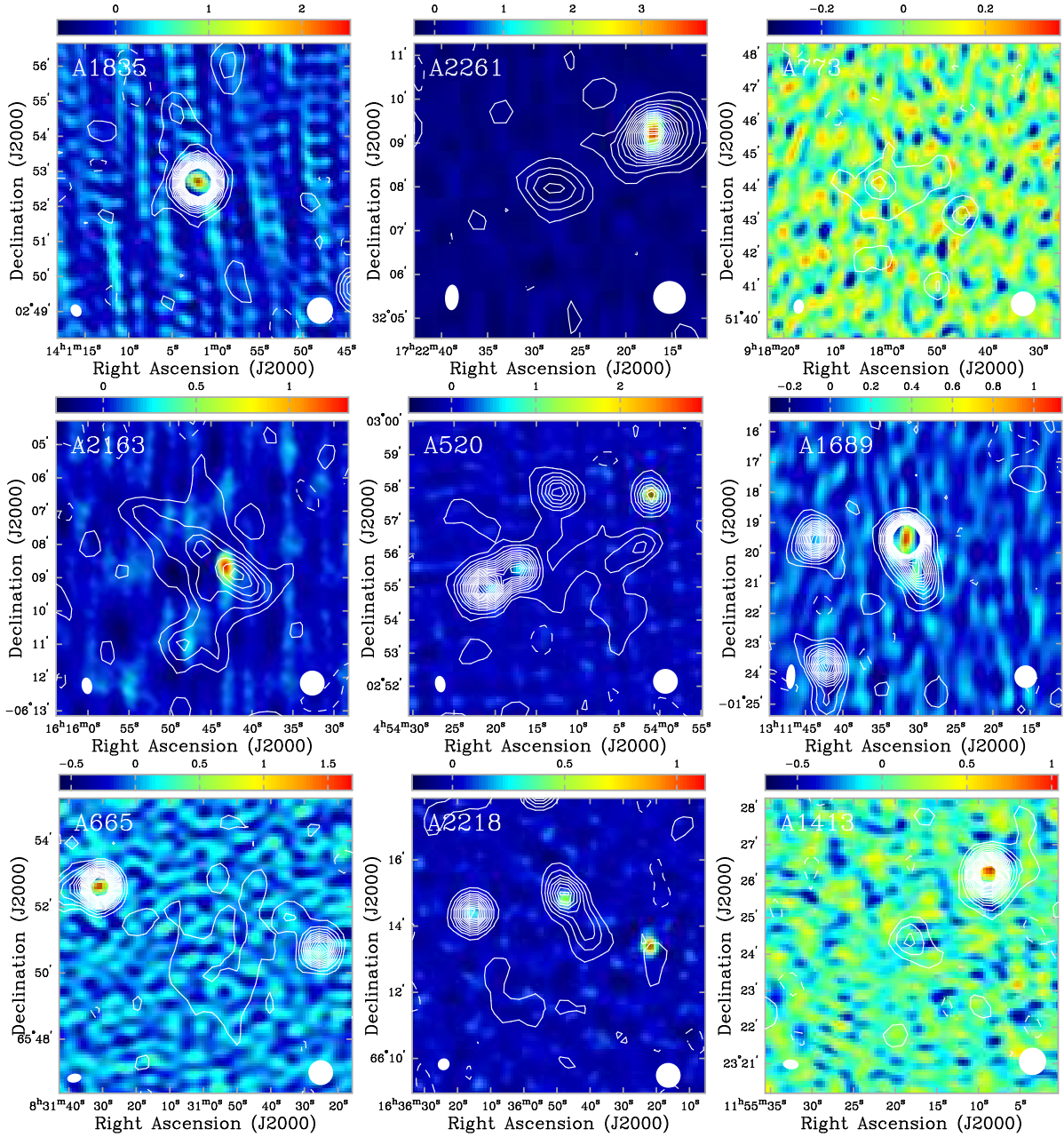


FIG. 1.—Cont.

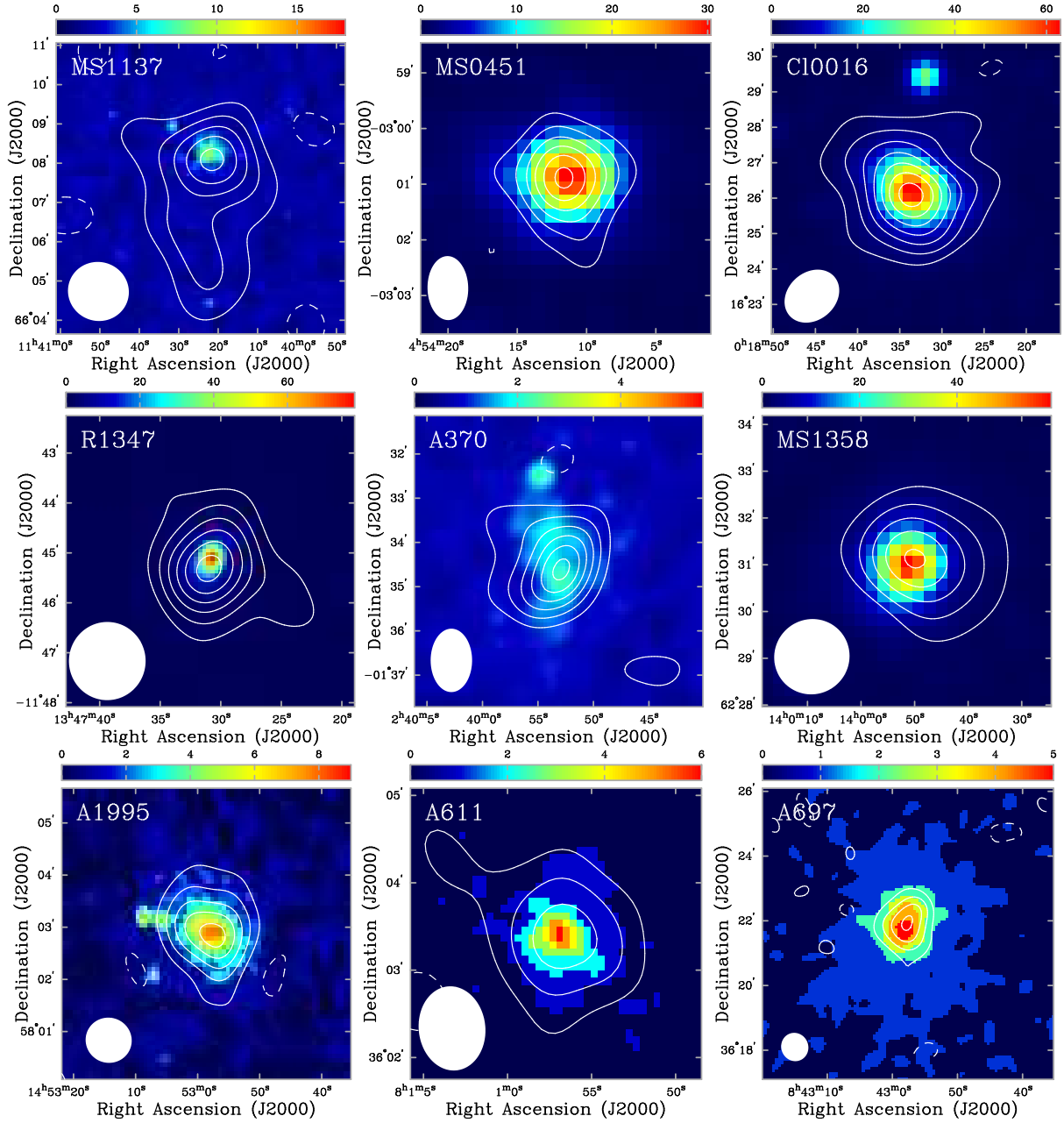


FIG. 2.—SZE (contours) and X-ray (color scale) images of each cluster in our sample. Negative contours are shown as solid lines. The contours are multiples of 2σ and the FWHM of the synthesized beams are shown in the bottom left corner. The X-ray color scale images are raw counts images smoothed with Gaussians with $\sigma = 15''$ for PSPC data and $\sigma = 5''$ for HRI data. There is a color scale mapping for the counts above each image. The 30 GHz image statistics are summarized in Table 4.

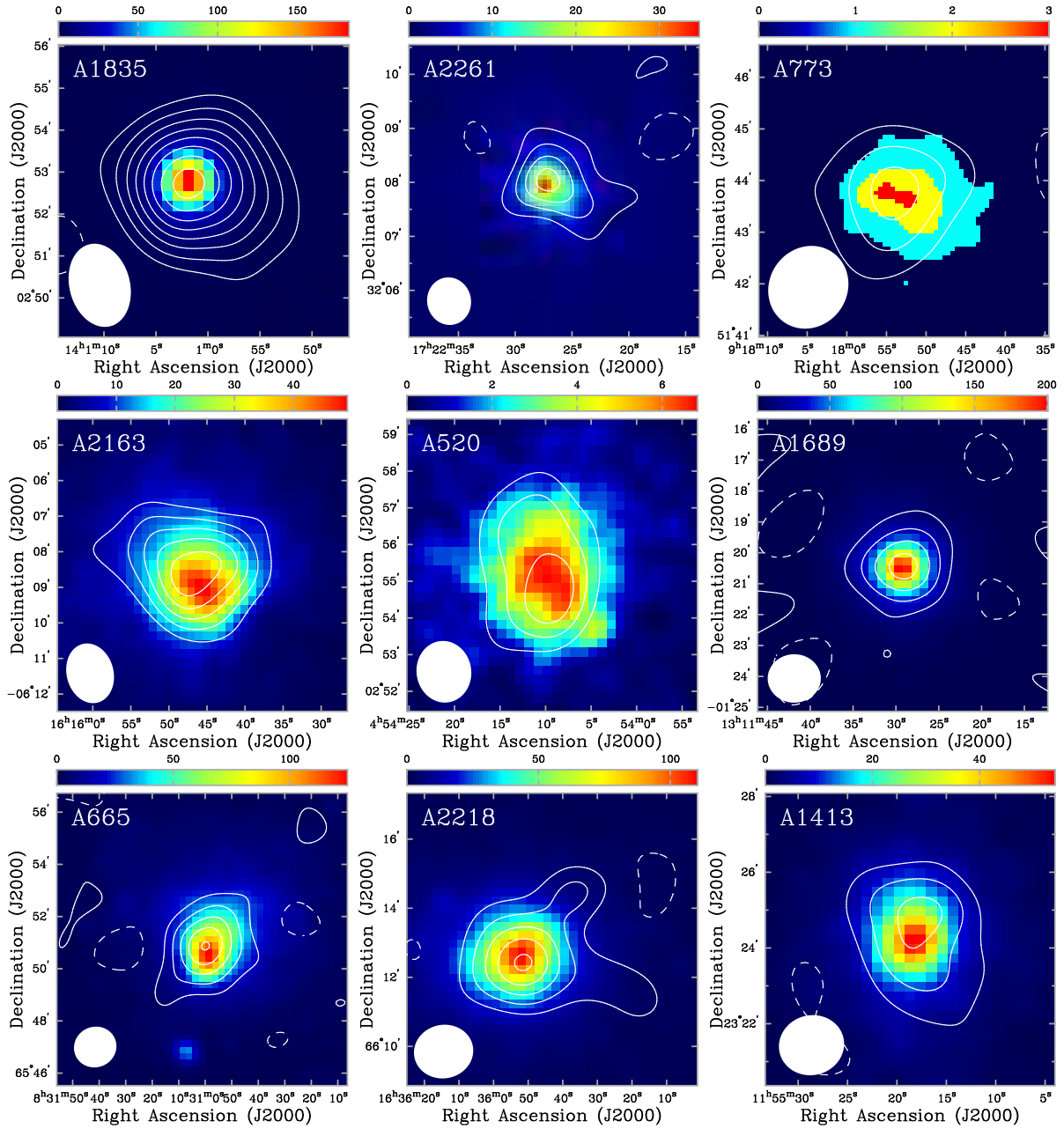


FIG. 2.—Cont.

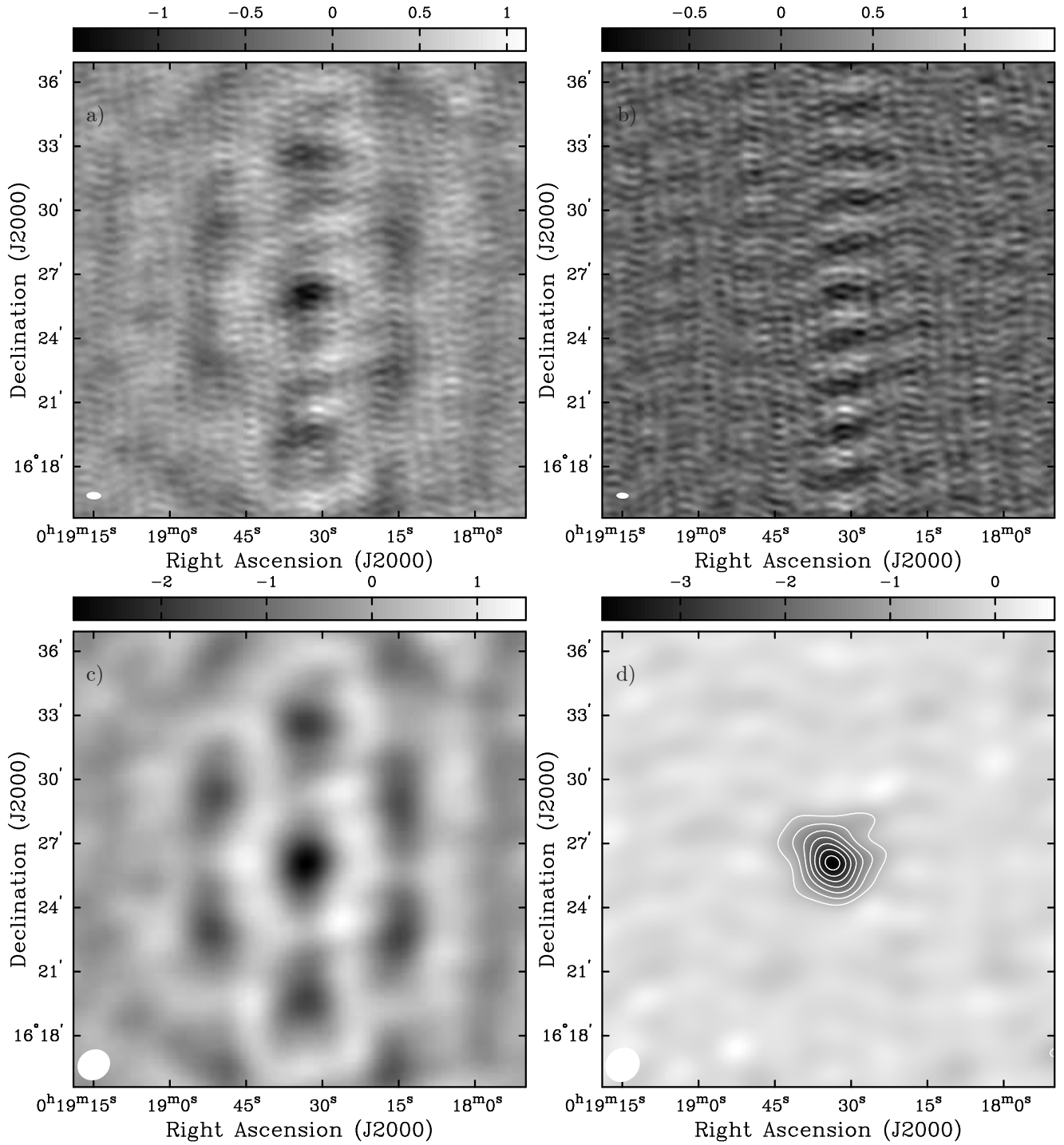


FIG. 3.—Panels illustrating how the spatial filtering of the interferometer is used to disentangle the point source emission from the SZE emission. Each panel is roughly 20' on a side with the FWHM of the synthesized beam shown in the lower left hand corner. The mapping of the color scale is shown above each panel in units of mJy beam⁻¹. Panels: *a*) “natural”; *b*) high resolution ($\geq 2000 \lambda$); *c*) tapered map after point source removal; and *d*) deconvolved SZE image (contours are multiples of 2 σ). See text for details.

for the HRI (0.1-2.4 keV) data and for each of the Snowden bands R4-R7 (PI channels 52 – 201; approximately 0.5 – 2.0 keV) for the PSPC data, using a master veto rate (a measure of the cosmic-ray and γ -ray backgrounds) of 200 counts s^{-1} for the PSPC data. We examine the light curve data of both instruments looking for time intervals with anomalously high count rates (short-term enhancements) and for periods of high scattered solar X-ray contamination. Contaminated and anomalously high count rate data are excised. The Snowden software produces 512×512 pixel images with $14''/947$ pixels for the PSPC and $5''/0$ pixels for the HRI. For the PSPC, final images for all of the R4-R7 bands together are generated by adding the raw counts images and the background images. Each Snowden band has a slightly different effective exposure map and there is an energy dependence in the point spread function (PSF). Thus, we generate a single exposure image and a single PSF image by combining cluster photon-weighted averages of the four exposure images and the four PROS (Worrall et al. 1992; Conroy et al. 1993) generated on-axis PSF images. The cluster photon-weighting is determined using the background subtracted detected photons within a circular region centered on the cluster. The region selected to construct the weights is the largest circular region encompassing the cluster which contains no bright point sources, typically a 15 pixel radius.

3.2.2. X-ray Images and Data Properties

We show smoothed X-ray raw counts images in Figure 2 (color) with SZE image contours overlaid. PSPC images are shown when available and HRI images otherwise. Table 2 summarizes the on-source integration time of the *ROSAT* observations of the clusters in our sample for both the PSPC and HRI. These images roughly contain a few thousand cluster counts. PSPC images are smoothed with Gaussians with $\sigma = 15''$ and HRI images with $\sigma = 5''$. The color scale wedge above each figure shows the mapping between color and detector counts.

3.2.3. X-ray Spectral Data

We used published temperatures, metallicities, and H I column densities from observations with the Advanced Satellite for Cosmology and Astrophysics (ASCA). Temperatures and metallicities for most of the clusters in our sample appear in Allen & Fabian (1998a), Allen & Fabian (1998b), and Allen (2000). When there is a detailed account of the analysis for a particular cluster we use those results instead. When fitted metallicities are unavailable, we adopt a 0.2 solar metallicity with a 100% uncertainty. We use fitted H I column densities when available, otherwise those from 21 cm surveys of our galaxy (Dickey & Lockman 1990) are adopted. We assign a conservative 50% uncertainty to the column densities adopted.

TABLE 4
SZE IMAGE STATISTICS

Cluster	Tapered ^a			High Resolution ^b			
	Observatory	σ ($\mu\text{Jy beam}^{-1}$)	Beam (arcsec)	σ_{RJ} (μK)	Observatory	σ ($\mu\text{Jy beam}^{-1}$)	Beam (arcsec)
MS1137	BIMA	120	90×94	21	BIMA	105	20×24
MS0451	OVRO	90	44×69	45	OVRO	60	19×25
C10016	BIMA	250	81×101	46	BIMA	220	14×30
R1347	BIMA	307 ^c	93×94^c	53 ^c	BIMA	245	17×27
A370	OVRO	60	56×86	19	OVRO	70	17×23
MS1358	BIMA	140	96×98	22	BIMA	120	17×20
A1995	BIMA	134	70×77	37	OVRO	65	17×20
A611	OVRO	60	48×58	32	OVRO	45	20×39
A697	OVRO	65	50×53	37	OVRO	50	19×33
A1835	BIMA	213	87×121	30	BIMA	190	18×22
A2261	OVRO	85	49×53	49	OVRO	75	19×35
A773	BIMA	260	91×99	43	OVRO	90	19×26
A2163	BIMA	300	90×104	48	OVRO	85	19×30
A520	BIMA	180	90×101	30	OVRO	80	12×16
A1689	BIMA	320	93×94	55	OVRO	72	18×49
A665	BIMA	160	93×99	26	BIMA	150	16×26
A2218	BIMA	200	93×99	31	OVRO	50	21×22
A1413	BIMA	250	93×99	44	BIMA	210	16×26

^aGaussian taper with FWHM of 2000 λ for OVRO data and 1000 λ for BIMA data.

^bUsing only data with $\sqrt{(u^2 + v^2)} > 2000 \lambda$.

^cUsed Gaussian taper with FWHM of 1500 λ .

from 21 cm surveys of our galaxy. Table 5 summarizes our adopted electron temperatures, metallicities, and column densities with references for the sources of this information.

Temperatures for many of our clusters also appear in Mushotzky & Scharf (1997). Multiple temperature determinations agree within the 1σ intervals for most of the clusters in our sample. The measurements overlap within 2σ in the worst cases, i.e., for the clusters, MS1358, A1995, A2163, A1689, and A1413. The temperatures, metallicity, column densities, and redshift of the cluster are used to determine the X-ray cooling functions and the conversion factor between detector counts and cgs units, Σ (see §3.2.4 below for details). The cooling functions and conversion factors are summarized in Table 6.

3.2.4. X-ray Cooling Function

The X-ray cooling function enters the distance calculation linearly and indirectly as the conversion between detector counts and cgs units (see §4.1). We use a Raymond-Smith (1977) spectrum to describe the hot ICM, which includes contributions from electron-ion thermal bremsstrahlung, line emission, recombination, and two photon processes. We replace the non-relativistic bremsstrahlung calculation in the Raymond-Smith model with the relativistic calculation of Gould (1980). A discussion of this calculation appears in Reese et al. (2000).

The cooling function results for the *ROSAT* data used in our analysis are summarized in Table 6, where Λ_{cH0} is the cooling function in cgs units, $\Lambda_{\text{eH0}}^{\text{det}}$ is the cooling function in detector units, Σ is the conversion between counts and cgs units, and Λ_{bol} is the bolometric cooling function. The cooling functions with relativistic corrections are typically 1.05 times the Raymond-Smith “uncorrected” value for the clusters in our sample.

TABLE 5
X-RAY SPECTRAL INFORMATION

cluster	kT_e (keV)	[Fe/H]	N_{H} ($\times 10^{20} \text{ cm}^{-2}$)	ref- T_e ; [Fe/H]; N_{H}
MS1137	$5.7^{+1.3}_{-0.7}$	$0.43^{+0.26}_{-0.24}$	1.00 ^a	D99;D99;D99
MS0451	$10.4^{+1.0}_{-0.8}$	$0.15^{+0.07}_{-0.07}$	$3.00^{+0.40}_{-0.30}$	D96;D96;D96
C10016	$7.55^{+0.72}_{-0.58}$	$0.07^{+0.11}_{-0.07}$	$5.59^{+0.41}_{-0.36}$	HB98;HB98;HB98
R1347	$9.3^{+0.7}_{-0.6}$	$0.33^{+0.06}_{-0.06}$	$10.00^{+4.00}_{-4.00}$	S97;S97;S97
A370	$6.6^{+0.7}_{-0.5}$	$0.3^{+0.1}_{-0.1}$	3.1 ^b	O98;O98;G
MS1358	$7.48^{+0.50}_{-0.42}$	$0.32^{+0.09}_{-0.09}$	1.93 ^b	AF98;AF98b;G
A1995	$8.59^{+0.86}_{-0.67}$	$0.14^{+0.07}_{-0.07}$	$5.0^{+1.6}_{-1.6}$	P00;P00;P00
A611	$6.6^{+0.6}_{-0.6}$	0.20 ^c	4.99 ^b	HPC;-;G
A697	$9.8^{+0.7}_{-0.7}$	0.20 ^c	3.41 ^b	HPC;-;G
A1835	$8.21^{+0.19}_{-0.17}$	$0.35^{+0.04}_{-0.03}$	2.32 ^b	AF98;AF98b;G
A2261	$8.82^{+0.37}_{-0.32}$	$0.32^{+0.06}_{-0.05}$	3.28 ^b	AF98;AF98b;G
A773	$9.29^{+0.41}_{-0.36}$	$0.21^{+0.05}_{-0.05}$	1.44 ^b	AF98;AF98b;G
A2163	$12.2^{+1.1}_{-0.7}$	$0.40^{+0.09}_{-0.08}$	$16.50^{+0.90}_{-1.14}$	M96;EAB95;EAB95
A520	$8.33^{+0.46}_{-0.40}$	$0.14^{+0.06}_{-0.06}$	7.80 ^b	AF98;AF98b;G
A1689	$9.66^{+0.22}_{-0.20}$	$0.29^{+0.03}_{-0.03}$	1.82 ^b	AF98;AF98b;G
A665	$9.03^{+0.35}_{-0.31}$	$0.22^{+0.04}_{-0.05}$	4.24 ^b	AF98,AF98b;G
A2218	$7.05^{+0.22}_{-0.21}$	$0.18^{+0.04}_{-0.04}$	3.24 ^b	AF98;AF98b;G
A1413	$7.54^{+0.17}_{-0.16}$	$0.28^{+0.03}_{-0.03}$	2.19 ^b	AF98;AF98b;G

^aAdopted value (see ref D99) and adopted 50% uncertainty.

^bGalactic value (Dickey & Lockman 1990) with adopted 50% uncertainty.

^cAdopted value with assumed 100% uncertainty.

NOTE: Uncertainties are 68% confidence.

REF: AF98-Allen & Fabian 1998a; AF98b-Allen & Fabian 1998b; D96-Donahue 1996; D99-Donahue et al. 1999; EAB95-Elbaz et al. 1995; G-Dickey & Lockman 1990; HPC-Hughes, private communication; HB98-Hughes & Birkinshaw 1998; M96-Markevitch et al. 1996; O98-Ota et al. 1998; P00-Patel et al. 2000; S97-Schindler et al. 1997

TABLE 6
X-RAY COOLING FUNCTIONS

cluster	Λ_{eH0} ^a	PSPC		HRI		$\frac{n_e}{n_H} = \frac{\mu_H}{\mu_e}$	Λ_{bol} ^d
		Λ_{eH0}^{det} ^b	Σ^c	Λ_{eH0}^{det} ^b	Σ^c		
MS1137	7.751	1.765	2.461	1.202	2.146
MS0451	6.948	3.263	1.373	1.470	3.050	1.198	2.702
Cl0016	6.922	3.003	1.489	1.289	3.471	1.197	2.260
R1347	6.922	1.167	4.089	1.201	2.643
A370	6.790	1.627	3.037	1.200	2.223
MS1358	6.717	3.785	1.336	1.793	2.821	1.200	2.371
A1995	6.434	1.434	3.395	1.198	2.448
A611	6.511	1.489	3.395	1.199	2.175
A697	6.334	1.570	3.148	1.199	2.647
A1835	6.462	3.839	1.344	1.775	2.909	1.201	2.496
A2261	6.359	1.649	3.150	1.200	2.570
A773	6.171	1.870	2.715	1.199	2.581
A2163	6.135	2.555	1.998	1.021	5.000	1.202	3.064
A520	6.119	3.209	1.586	1.337	3.807	1.198	2.411
A1689	6.158	3.899	1.335	1.835	2.836	1.200	2.673
A665	6.102	3.616	1.428	1.570	3.289	1.199	2.550
A2218	6.112	3.789	1.378	1.691	3.086	1.198	2.237
A1413	6.133	4.000	1.343	1.856	2.894	1.200	2.361

^aUnits are $\times 10^{-24}$ erg s⁻¹ cm³. The emissivity in the cluster frame integrated over the ROSAT band (0.5-2.0 keV) redshifted to the cluster frame.

^bUnits are $\times 10^{-13}$ cnts s⁻¹ cm⁵. The emissivity in the detector frame accounting for the response of the instrument.

^cUnits are $\times 10^{-11} \frac{\text{erg s}^{-1} \text{cm}^{-2}}{\text{cnt s}^{-1}}$. The conversion of detector units to cgs units including the $(1+z)$ factor between energy and counts.

^dUnits are $\times 10^{-23}$ erg s⁻¹ cm³. The bolometric emissivity.

4. METHOD

4.1. Angular Diameter Distance Calculation

The calculation begins by constructing a model for the cluster gas distribution. We use a spherical isothermal β model to describe the ICM. With this model, the cluster's extent along the line of sight is the same as that in the plane of the sky. This is clearly invalid in the presence of cluster asphericities. Thus cluster geometry introduces an important uncertainty in SZE and X-ray derived distances. In general, clusters are dynamically young, are aspherical, and rarely exhibit projected gas distributions which are circular on the sky (Mohr et al. 1995). We currently cannot disentangle the complicated cluster structure and projection effects, but numerical simulations provide a good base for understanding these difficulties. The effects of asphericity contribute significantly to the distance uncertainty for each cluster, but are not believed to result in any significant bias in the Hubble parameter derived from a large sample of clusters (Sulkanen 1999).

The spherical isothermal β model has the form (Cavaliere & Fusco-Femiano 1976, 1978)

$$n_e(\mathbf{r}) = n_{e0} \left(1 + \frac{r^2}{r_c^2} \right)^{-3\beta/2}, \quad (1)$$

where n_e is the electron number density, r is the radius from the center of the cluster, r_c is the core radius of the ICM, and β is the power law index. With this model, the SZE signal is

$$\Delta T = f_{(x,T_e)} T_{\text{CMB}} D_A \int d\zeta \sigma_T n_e \frac{k_B T_e}{m_e c^2} = \Delta T_0 \left(1 + \frac{\theta^2}{\theta_c^2} \right)^{(1-3\beta)/2}, \quad (2)$$

where ΔT is the thermodynamic SZE temperature decrement/increment, $f_{(x,T_e)}$ is the frequency dependence of the SZE with $x = h\nu/kT_{\text{CMB}}$, T_{CMB} (=2.728 K; Fixsen et al. 1996) is the temperature of the CMB radiation, k_B is the Boltzmann constant, σ_T is the Thompson cross section, m_e is the mass of the electron, c is the speed of light, ΔT_0 is the central thermodynamic SZE temperature decrement/increment, θ is the angular radius in the plane of the sky and θ_c the corresponding angular core radius, and the integration is along the line of sight $\ell = D_A \zeta$. The frequency dependence of the thermal SZE is

$$f_{(x,T_e)} = \left(x \frac{e^x + 1}{e^x - 1} - 4 \right) (1 + \delta_{\text{SZE}}(x, T_e)) \quad (3)$$

where $\delta_{\text{SZE}}(x, T_e)$ is the relativistic correction to the frequency dependence. In the non-relativistic and Rayleigh-Jeans (R.J) limits, $f_{(x,T_e)} \rightarrow -2$. We apply the relativistic corrections $\delta_{\text{SZE}}(x, T_e)$ to fifth order in $kT_e/m_e c^2$ (Itoh et al. 1998), which agrees with other works (Rephaeli 1995; Rephaeli & Yankovitch 1997; Stebbins 1997; Challinor & Lasenby 1998; Sazonov & Sunyaev 1998a,b; Molnar & Birkinshaw 1999; Dolgov et al. 2001) for clusters with $k_B T_e \leq 15$ keV, satisfied by all the clusters in our sample. This correction decreases the magnitude of $f_{(x,T_e)}$ by $\lesssim 5\%$ (typically 3%) for the clusters considered here.

The X-ray surface brightness is

$$S_x = \frac{1}{4\pi(1+z)^4} D_A \int d\zeta n_e n_H \Lambda_{eH} = S_{x0} \left(1 + \frac{\theta^2}{\theta_c^2} \right)^{(1-6\beta)/2}, \quad (4)$$

where S_x is the X-ray surface brightness in cgs units ($\text{erg s}^{-1} \text{cm}^{-2} \text{arcmin}^{-2}$), z is the redshift of the cluster, n_H is the hydrogen number density of the ICM, $\Lambda_{eH} = \Lambda_{eH}(T_e, \text{abundance})$ is the X-ray cooling function of the ICM in the cluster rest frame in cgs units ($\text{erg cm}^3 \text{s}^{-1}$) integrated over the redshifted *ROSAT* band, and S_{x0} is the X-ray surface brightness in cgs units at the center of the cluster. Since the X-ray observations are in instrument counts, we also need the conversion factor between detector counts and cgs units, Σ ($S_{x0} = S_{x0}^{\text{det}} \Sigma$), discussed in detail in Reese et al. (2000) along with a description of the calculation of Λ_{eH} , which includes relativistic corrections (Gould 1980) to the Raymond & Smith (1977) spectrum. The normalizations, ΔT_0 and S_{x0} , used in the fit include all of the physical parameters and geometric terms that come from the integration of the β model along the line of sight.

One can solve for the angular diameter distance by eliminating n_{e0} (noting that $n_H = n_e \mu_e / \mu_H$ where $n_j \equiv \rho / \mu_j m_p$ for species j) yielding

$$D_A = \frac{(\Delta T_0)^2}{S_{x0}} \left(\frac{m_e c^2}{k_B T_{e0}} \right)^2 \frac{\Lambda_{eH0} \mu_e / \mu_H}{4\pi^{3/2} f_{(x,T_e)}^2 T_{\text{CMB}}^2 \sigma_T^2 (1+z)^4 \theta_c} \frac{1}{\theta_c} \left[\frac{\Gamma(\frac{3}{2}\beta)}{\Gamma(\frac{3}{2}\beta - \frac{1}{2})} \right]^2 \frac{\Gamma(3\beta - \frac{1}{2})}{\Gamma(3\beta)} \quad (5)$$

where $\Gamma(x)$ is the Gamma function. Similarly, one can eliminate D_A instead and solve for the central density n_{e0} .

More generally, the angular diameter distance is

$$D_A = \frac{(\Delta T_0)^2}{S_{x0}} \left(\frac{m_e c^2}{k_B T_{e0}} \right)^2 \frac{\Lambda_{eH0} \mu_e / \mu_H}{4\pi f_{(x,T_e)}^2 T_{\text{CMB}}^2 \sigma_T^2 (1+z)^4 \theta_c} \frac{1}{\theta_c} \frac{\int \left(\frac{n_e}{n_{e0}} \right)^2 \frac{\Lambda_{eH}}{\Lambda_{eH0}} d\eta \big|_{R=0}}{\left[\int \frac{n_e}{n_{e0}} \frac{T_e}{T_{e0}} d\eta \big|_{R=0} \right]^2}, \quad (6)$$

where θ_c is the characteristic angular scale of the galaxy cluster whose exact meaning depends on the ICM model (the core radius for the isothermal β model) and $\eta \equiv \zeta / \theta_c \equiv \ell / r_c$ is the line of sight length in units of the characteristic radius, $r_c = \theta_c D_A$. For simplicity in notation, we have assumed that the density and temperature models are normalized at the central value (denoted with 0) though any location for the normalization is allowed. The above integrals are along the central line of sight, denoted as zero projected radius $R = 0$. The Γ functions and the factor of $\pi^{1/2}$ in equation (5) come from the integration of the β model along the central line of sight for both the SZE and X-ray models.

4.2. Joint SZE and X-ray Model Fitting

The SZE and X-ray emission both depend on the properties of the ICM, so a joint fit to the interferometric SZE data and the PSPC and HRI X-ray data provides the best constraints on those properties. Each data set is assigned a collection of parameterized models. Typically, SZE data sets are assigned a β model and point sources and X-ray images are assigned a β model and a cosmic X-ray background model. This set of models is combined for each data set to create a composite model which is then compared to the data.

Our analysis procedure is described in detail in Reese et al. (2000). The philosophy behind the analysis is to keep the data in a reduced but “raw” state and run the model through the observing strategy to compare directly with the data. In particular, the interferometric SZE observations provide constraints in the Fourier (u - v) plane, so we perform our model fitting in the u - v plane, where the noise properties of the data and the spatial filtering of the interferometer are well defined. The SZE model is generated in the image plane, multiplied by the primary beam, and fast Fourier transformed to produce model visibilities. We then interpolate the model visibilities to the u and v of each data visibility and compute the Gaussian likelihood. For X-ray data, the model is convolved with the appropriate point spread function and the Poisson likelihood is computed pixel by pixel, ignoring the masked point source regions.

Each data set is independent, and likelihoods from each data set can simply be multiplied together to construct the joint likelihood. Likelihood ratio tests can then be performed to get confidence regions or compare two models. Rather than working directly with likelihoods, \mathcal{L} , we work with $S \equiv -2 \ln(\mathcal{L})$. We then construct a $\Delta\chi^2$ -like statistic from the log likelihoods, $\Delta S \equiv S_n - S_{min}$ where S_{min} is the minimum of the S function and S_n is the S statistic where n parameters differ from the parameters at S_{min} . The statistic ΔS is sometimes referred to as the Cash (1979) statistic and tends to a χ^2 distribution with n degrees of freedom for large n (Kendall & Stuart 1979, for example). This ΔS statistic is equivalent to the likelihood ratio test and is used to generate confidence regions and confidence intervals. For one interesting parameter, the 68.3% ($\sim 1\sigma$) confidence level corresponds to $\Delta S = 1.0$.

4.2.1. Model Fitting Uncertainty Estimation

Uncertainties in the angular diameter distance from the fit parameters are calculated by varying the interesting parameters to explore the ΔS likelihood space. The most important parameters in this calculation are ΔT_0 , S_{x0} , β , and θ_c . Radio point sources and the cosmic X-ray background affect ΔT_0 and S_{x0} , respectively. As a compromise between precision and computation time, we systematically vary ΔT_0 , S_{x0} , β , and θ_c allowing the X-ray backgrounds for the PSPC and HRI to float independently while fixing the positions of the cluster (both SZE and X-ray), and the positions and flux densities of any radio point sources in the SZE cluster fields. We describe our estimation of the effects of point sources below.

From this four dimensional ΔS hyper-surface, we construct confidence intervals for each parameter individually as well as confidence intervals for D_A due to S_{x0} , ΔT_0 , β , and θ_c jointly. To compute the 68.3% confidence region we find the minimum and maximum values of the parameter within a ΔS of 1.0. We emphasize that these uncertainties are meaningful only within the context of the spherical isothermal β model.

Measured Radio Point Sources

Two methods of estimating the effect of the measured radio point sources in the cluster field are examined, one which is reasonably quick and one that is more rigorous. For the quick estimate, we first determine the 1σ confidence limits on the flux density of each point source by varying the point source flux density while keeping the ICM parameters fixed at their best fit values. These are the uncertainties listed in Table 3, after correcting for the primary beam attenuation appropriate for each point source’s distance from the pointing center. We then determine the change in the central decrement over the 68.3% confidence region for the point source flux densities by fixing the point source flux density at the $\pm 1\sigma$ values and varying ΔT_0 while fixing the ICM shape parameters at their best fit values. This is done for each point source in the field and all combinations of the $\pm 1\sigma$ flux densities for fields with multiple point sources. We adopt the maximum percentage change in ΔT_0 as our uncertainty from radio point sources on the central decrement. The above procedure will be referred to as the quick estimate of the effects of measured radio point sources. We tested this estimate against marginalizing over the point source flux density by varying θ_c , β , S_{x0} , ΔT_0 , and point source flux for each point source, while fixing the X-ray background (simply saves computation time by isolating the point source flux issue). From the marginalized likelihood function we find the best fit and 68.3% uncertainty on ΔT_0 and D_A . The uncertainty from measured radio point sources, σ_{pt} , is computed assuming the uncertainties add in quadrature from

$$\sigma_{pt}^2 = \sigma_{mar}^2 - \sigma_{fix}^2, \quad (7)$$

where σ_{mar} and σ_{fix} are the uncertainties from the marginalized grids and the initial, point source fixed grids, respectively. Marginalizing over point source flux density was performed on two clusters with one point source each, A2261 and MS1358, and one cluster with two point sources, A1835. The quick estimation of the effects of point sources agrees to within 2% on D_A (1% on ΔT_0) with the marginalized likelihood analysis, just slightly over estimating the uncertainty due to point sources. The marginalization procedure is computationally intensive. Therefore, to save computation time, we use the quick procedure to estimate the effects of detected point sources on the central decrement.

As an additional test, we explore the maximum likelihood parameter space (varying θ_c , β , S_{x0} , and ΔT_0) with the point source fluxes fixed at the $\pm 1\sigma$ values for our three test case clusters: A2261, MS1358, and A1835. The effects of point sources on the central decrement from this study agree within a few percent with both the quick and marginalized

procedures. This is what was originally done for MS0451 and Cl0016 (Reese et al. 2000), which is now shown to give essentially the same result as marginalizing over the point source flux. For all clusters, we use the updated, quick estimates of the effects of measured point sources.

4.3. Model Fitting Results

We apply the analysis procedure described above to all 18 of our galaxy clusters. The results from our maximum likelihood joint fit to the SZE and X-ray data are summarized in Table 7, which shows the best-fit ICM shape parameters and the uncertainties on each parameter from the model fit.

So far, we have only shown the SZE data in the form of images though the data are recorded as visibilities. Figure 4 shows the SZE u - v radial profiles for Cl0016 with a series of 3 panels illustrating the features of such profiles. These profiles are azimuthal averages in the Fourier plane plotted as a function of the radius in the u - v plane, $\sqrt{u^2 + v^2}$. The data are the points with error bars and the best fit β model from the joint SZE and X-ray analysis is the solid line averaged the same way as the data. The point sources are subtracted directly from the visibilities before constructing the u - v radial profiles. All of these panels are shown on the same scale for easy comparison. Also plotted are the residuals in units of the standard deviation, $\Delta V/\sigma = (\text{data} - \text{model})/\sigma$. For a circular cluster at the phase center (coincident with the pointing center), one expects a monotonic real component and a zero imaginary component. Clusters are rarely exactly centered at the phase/pointing center of our observations. Therefore, we shift the phase center to the cluster center before constructing the u - v radial profiles. The phase shifted radial profiles are shown in the upper panel of Figure 4 for both the real (left) and imaginary (right) components of the complex visibilities. The model provides a good fit to the data for a wide range of spatial frequencies. The middle panel shows the u - v radial profile when the phase center is not shifted to the center of the cluster. The off-center cluster introduces corrugation in the Fourier plane modifying the expected real component and introducing a non-zero imaginary component. In addition, asymmetry in the cluster will manifest itself as a non-zero imaginary component. Our model is symmetric and its imaginary component should be identically zero. The attenuation from the primary beam introduces asymmetry, producing a non-zero imaginary component. This is illustrated in the lower panel of Figure 4 showing the u - v radial profile including the phase center shift but not including the primary beam correction when computing the model. Notice the model is identically zero unlike the upper panel, where the asymmetry produced by the primary beam on the off-center cluster shows a small imaginary component.

The u - v radial profiles for the real and imaginary components of the complex visibilities for each cluster in our sample are shown in Figure 5. Any point sources in the field are subtracted directly from the visibilities and the phase center

TABLE 7
ICM PARAMETERS

Cluster	β	θ_c (arcsec)	S_{x0}^{det} (detector) ^a	S_{x0} (cgs) ^b	ΔT_0 (μK)	D_A (Mpc)
MS1137	$0.786^{+0.220}_{-0.120}$	$19.4^{+6.4}_{-4.0}$	$1.80^{+0.30}_{-0.24} \times 10^{-2}$	$4.43^{+0.74}_{-0.59} \times 10^{-13}$	-818^{+98}_{-113}	3179^{+1103}_{-1640}
MS0451	$0.806^{+0.052}_{-0.043}$	$34.7^{+3.9}_{-3.5}$	$6.96^{+0.63}_{-0.61} \times 10^{-2}$	$9.56^{+0.86}_{-0.84} \times 10^{-13}$	-1431^{+98}_{-93}	1278^{+265}_{-299}
Cl0016	$0.749^{+0.024}_{-0.018}$	$42.3^{+2.4}_{-2.0}$	$4.14^{+0.15}_{-0.19} \times 10^{-2}$	$6.17^{+0.22}_{-0.28} \times 10^{-13}$	-1242^{+105}_{-105}	2041^{+484}_{-514}
R1347	$0.604^{+0.011}_{-0.012}$	$9.0^{+0.5}_{-0.5}$	$6.70^{+0.39}_{-0.34} \times 10^{-1}$	$2.74^{+0.16}_{-0.14} \times 10^{-11}$	-3950^{+350}_{-350}	1221^{+368}_{-343}
A370	$0.518^{+0.090}_{-0.080}$	$39.5^{+10.5}_{-10.5}$	$8.88^{+1.41}_{-0.99} \times 10^{-3}$	$2.70^{+0.43}_{-0.30} \times 10^{-13}$	-1253^{+218}_{-533}	4352^{+1388}_{-1245}
MS1358	$0.622^{+0.015}_{-0.015}$	$18.2^{+1.4}_{-1.5}$	$1.27^{+0.11}_{-0.08} \times 10^{-1}$	$1.70^{+0.15}_{-0.11} \times 10^{-12}$	-784^{+90}_{-90}	866^{+248}_{-310}
A1995	$0.770^{+0.117}_{-0.063}$	$38.9^{+6.9}_{-4.3}$	$3.18^{+0.24}_{-0.21} \times 10^{-2}$	$1.08^{+0.08}_{-0.07} \times 10^{-12}$	-1023^{+83}_{-77}	1119^{+247}_{-282}
A611	$0.565^{+0.050}_{-0.040}$	$17.5^{+3.5}_{-3.5}$	$5.91^{+1.06}_{-0.76} \times 10^{-2}$	$2.01^{+0.36}_{-0.26} \times 10^{-12}$	-853^{+120}_{-140}	995^{+325}_{-293}
A697	$0.540^{+0.045}_{-0.035}$	$37.8^{+5.6}_{-4.0}$	$3.24^{+0.22}_{-0.25} \times 10^{-2}$	$1.02^{+0.07}_{-0.08} \times 10^{-12}$	-1410^{+160}_{-180}	998^{+298}_{-250}
A1835	$0.595^{+0.007}_{-0.005}$	$12.2^{+0.6}_{-0.5}$	$1.50^{+0.10}_{-0.07} \times 10^{-0}$	$2.02^{+0.14}_{-0.10} \times 10^{-11}$	-2502^{+150}_{-175}	1027^{+194}_{-198}
A2261	$0.516^{+0.014}_{-0.013}$	$15.7^{+1.2}_{-1.1}$	$1.37^{+0.08}_{-0.08} \times 10^{-1}$	$4.31^{+0.26}_{-0.26} \times 10^{-12}$	-1697^{+200}_{-200}	1049^{+306}_{-272}
A773	$0.597^{+0.064}_{-0.032}$	$45.0^{+7.0}_{-5.0}$	$3.05^{+0.24}_{-0.24} \times 10^{-2}$	$8.28^{+0.65}_{-0.65} \times 10^{-13}$	-1260^{+160}_{-160}	1450^{+361}_{-332}
A2163	$0.674^{+0.011}_{-0.008}$	$87.5^{+2.5}_{-2.0}$	$6.82^{+0.15}_{-0.15} \times 10^{-2}$	$1.36^{+0.03}_{-0.03} \times 10^{-12}$	-1900^{+140}_{-140}	828^{+181}_{-205}
A520	$0.844^{+0.040}_{-0.040}$	$123.3^{+8.0}_{-8.0}$	$2.57^{+0.11}_{-0.11} \times 10^{-2}$	$4.08^{+0.18}_{-0.18} \times 10^{-13}$	-662^{+95}_{-95}	723^{+270}_{-236}
A1689	$0.609^{+0.005}_{-0.005}$	$26.6^{+0.7}_{-0.7}$	$4.50^{+0.13}_{-0.11} \times 10^{-1}$	$6.01^{+0.18}_{-0.15} \times 10^{-12}$	-1729^{+105}_{-120}	688^{+172}_{-163}
A665	$0.615^{+0.006}_{-0.006}$	$71.7^{+1.5}_{-1.5}$	$4.75^{+0.08}_{-0.08} \times 10^{-2}$	$6.78^{+0.12}_{-0.12} \times 10^{-13}$	-728^{+150}_{-150}	466^{+217}_{-179}
A2218	$0.692^{+0.008}_{-0.008}$	$67.5^{+1.3}_{-1.8}$	$5.14^{+0.12}_{-0.10} \times 10^{-2}$	$7.08^{+0.16}_{-0.14} \times 10^{-13}$	-731^{+125}_{-100}	1029^{+339}_{-352}
A1413	$0.639^{+0.009}_{-0.009}$	$47.7^{+2.0}_{-2.0}$	$1.52^{+0.07}_{-0.07} \times 10^{-1}$	$2.04^{+0.09}_{-0.09} \times 10^{-12}$	-856^{+110}_{-110}	573^{+171}_{-151}

^aUnits are $\text{cnt s}^{-1} \text{ arcmin}^{-2}$.

^bUnits are $\text{erg s}^{-1} \text{ cm}^{-2} \text{ arcmin}^{-2}$.

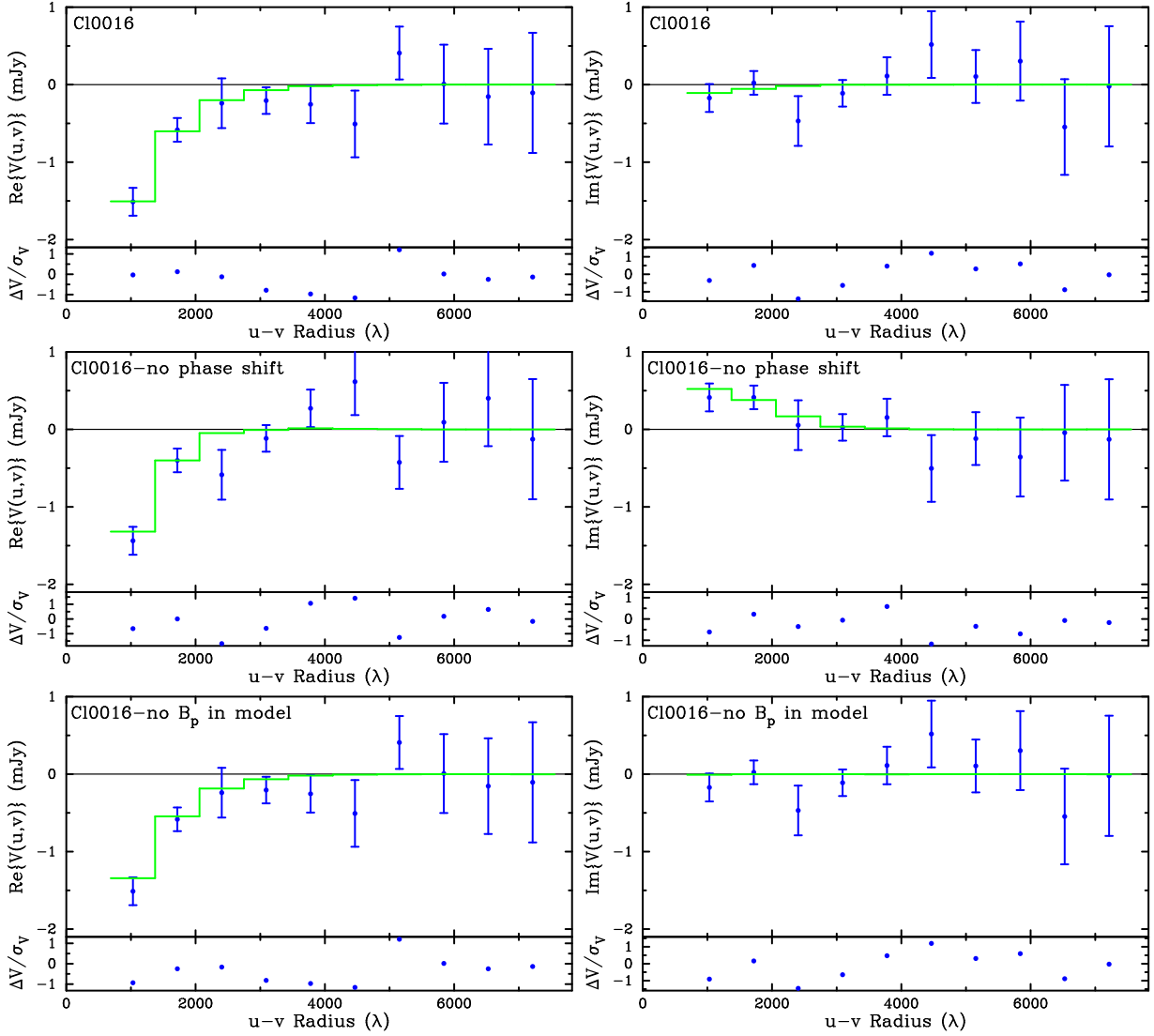


FIG. 4.—The real and imaginary components of the complex visibilities plotted as a function of radius in the u - v plane for Cl0016. The points with error bars are the data and the best fit model from the joint SZE and X-ray analysis is the solid line, averaged the same way as the data. Residuals are shown in units of the standard deviation. Shown are the phase shifted and primary beam corrected (upper panel), not phase shifted (middle panel), and not corrected for primary beam (lower panel) versions. Not shifting the phase center to the center of the cluster (middle panel) shows an imaginary component from this offset. Not applying the primary beam attenuation to the model after shifting the phase to the center of the cluster (lower panel) shows the expected zero imaginary component; a real and symmetric image should have a real only Fourier transform. The asymmetry induced by the primary beam correction for the off-center cluster introduces a small imaginary component (see upper panel).

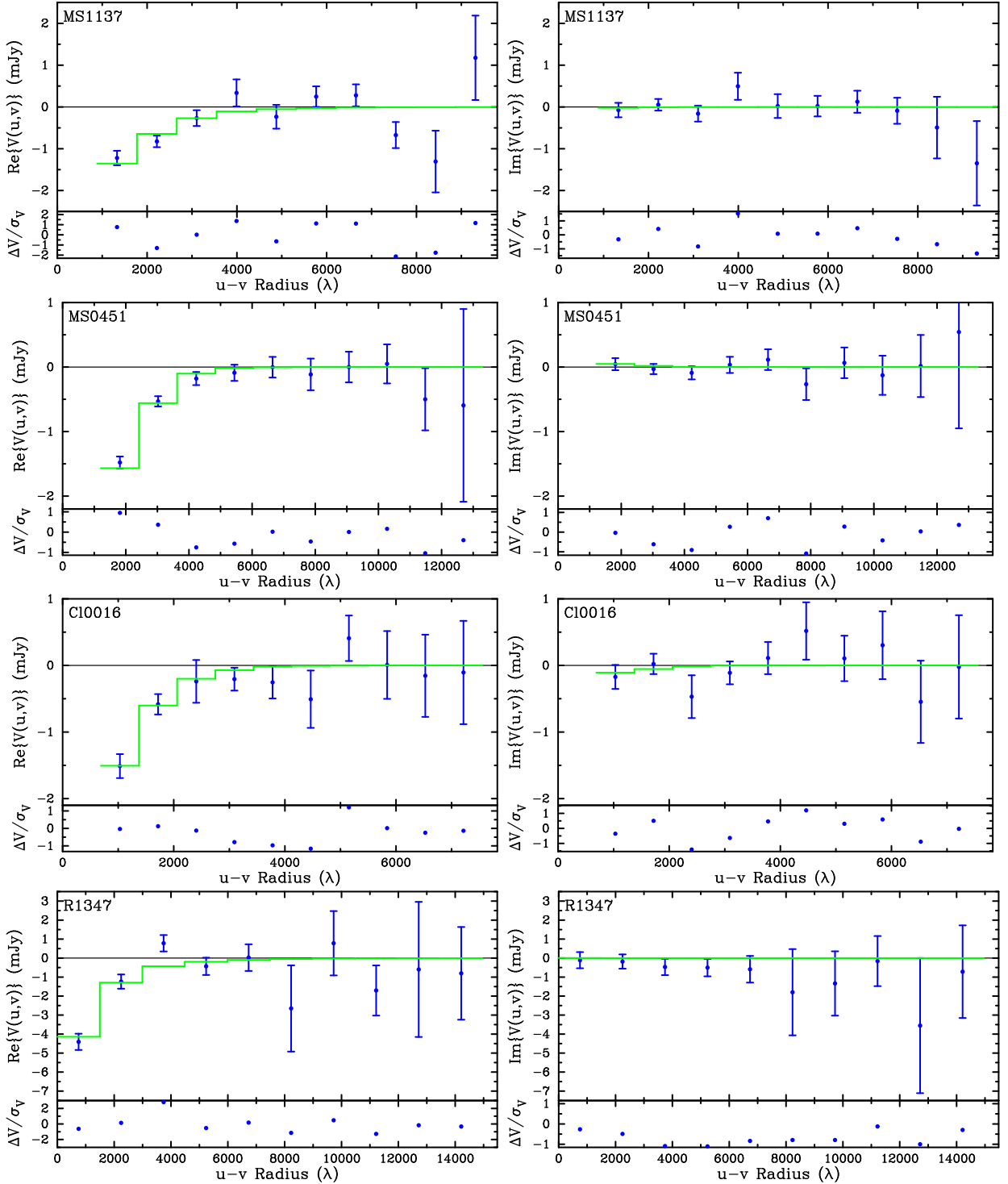


FIG. 5.—The real and imaginary components of the complex visibilities plotted as a function of radius in the u - v -plane. The points and error bars are the data and the solid line is the best fit model. Residuals are shown in units of the standard deviation. Any point sources in the cluster field have been subtracted directly from the visibilities and the phase center of the map has been shifted to the center of the cluster before making these radial averages. Non-zero signal in the imaginary components is due to the asymmetry in the cluster and the possible asymmetry introduced by the primary beam correction. The models provide good fits to the data for all the clusters in our sample.

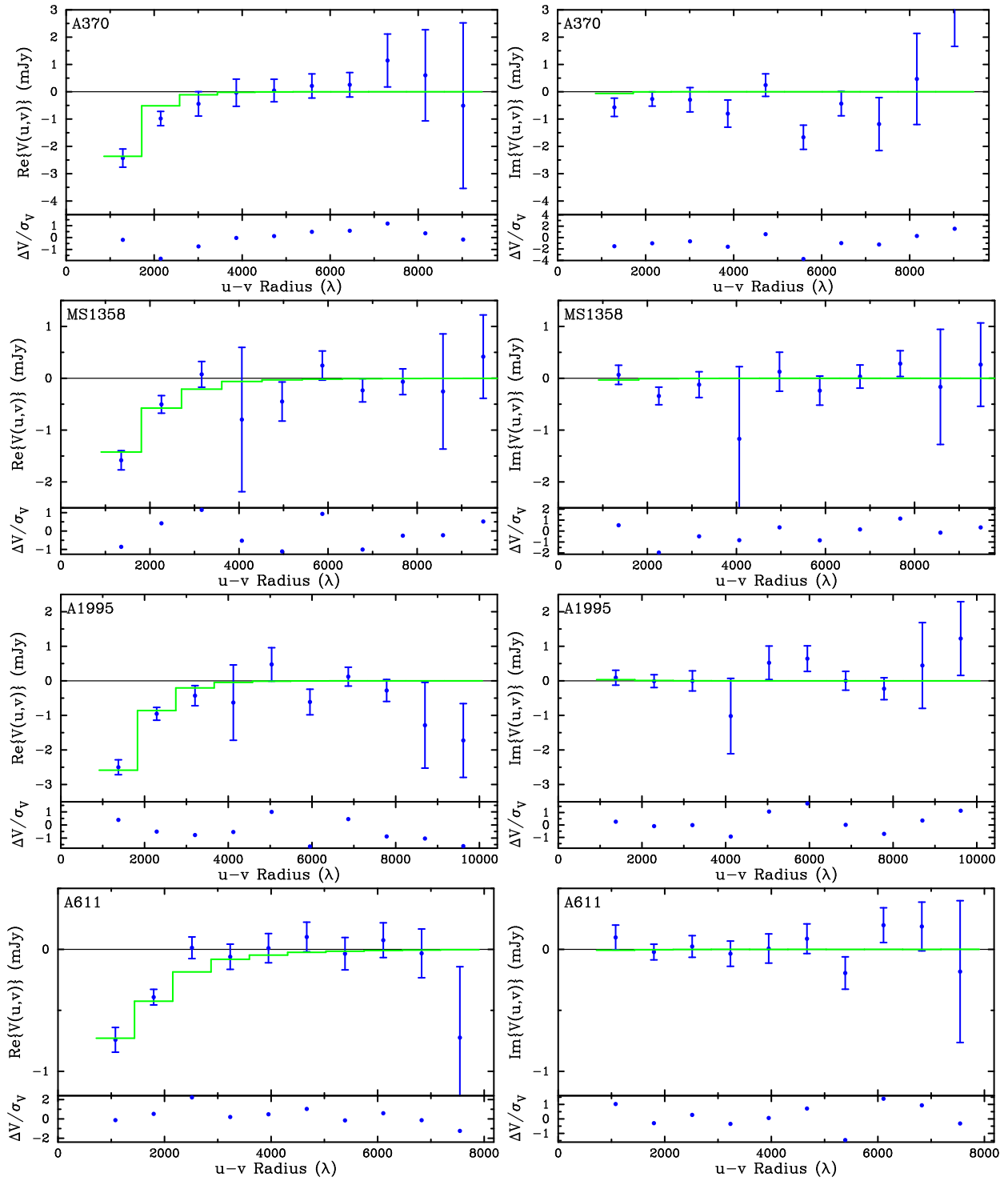


FIG. 5.—Cont.

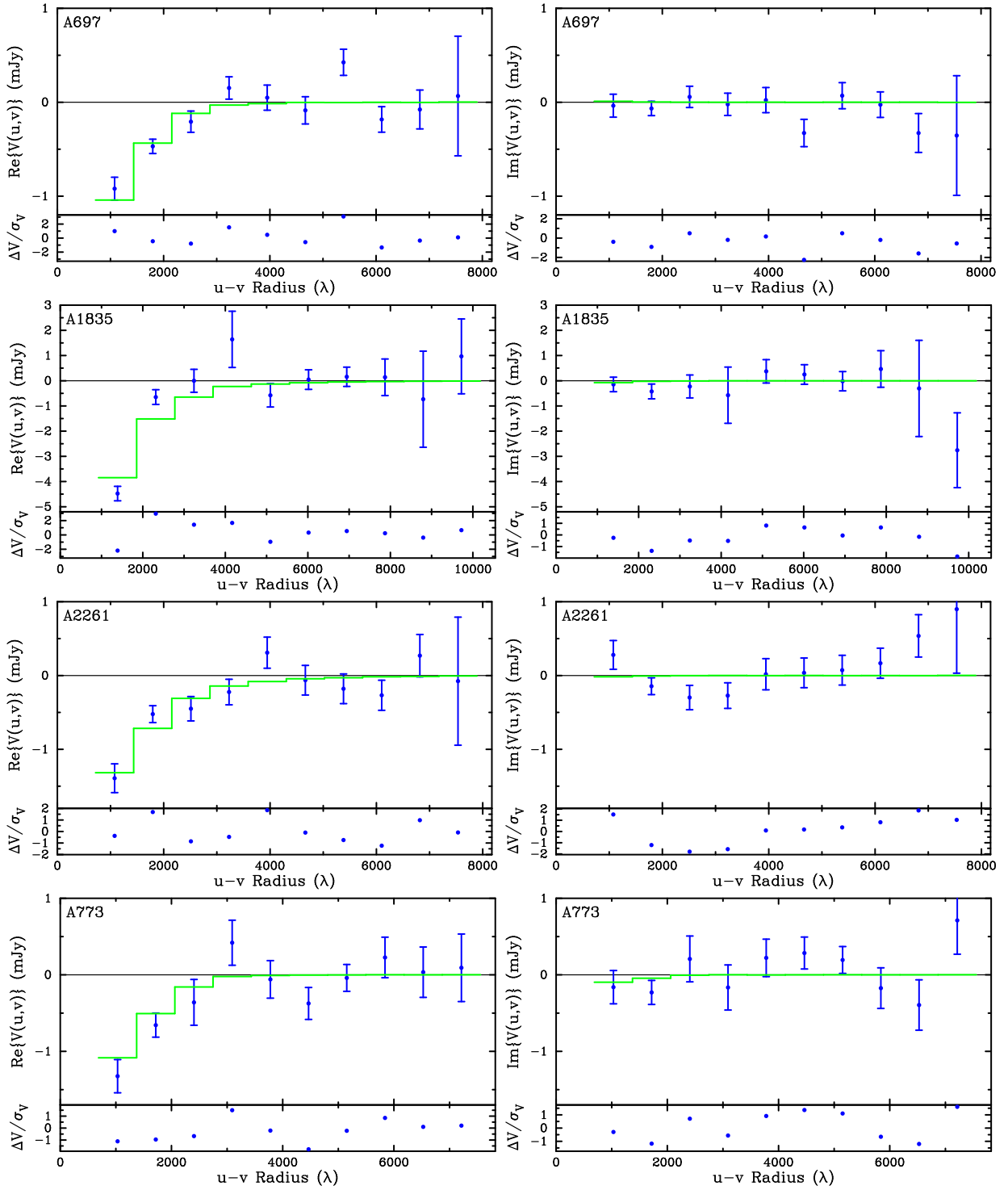


FIG. 5.—Cont.

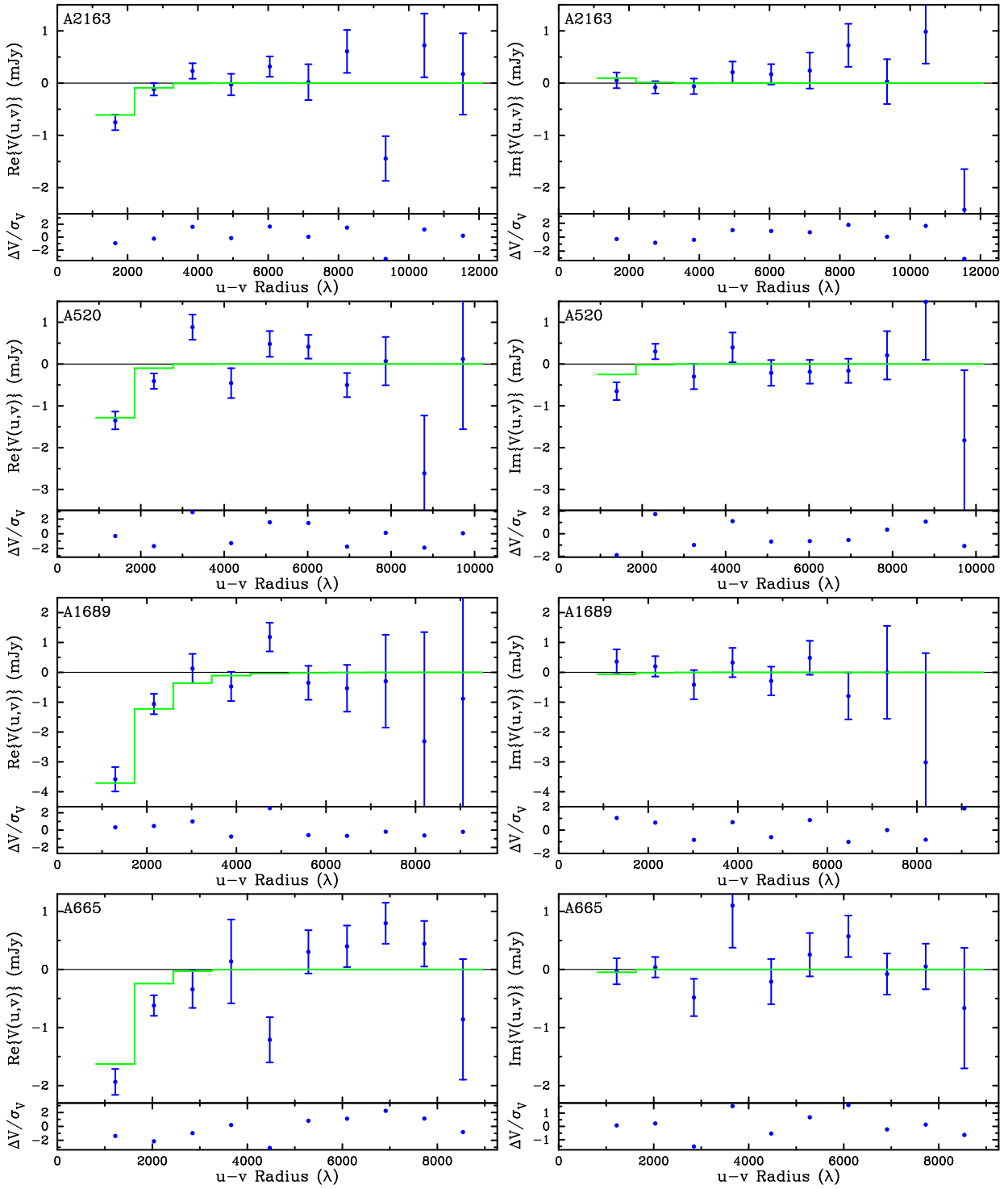


FIG. 5.—Cont.

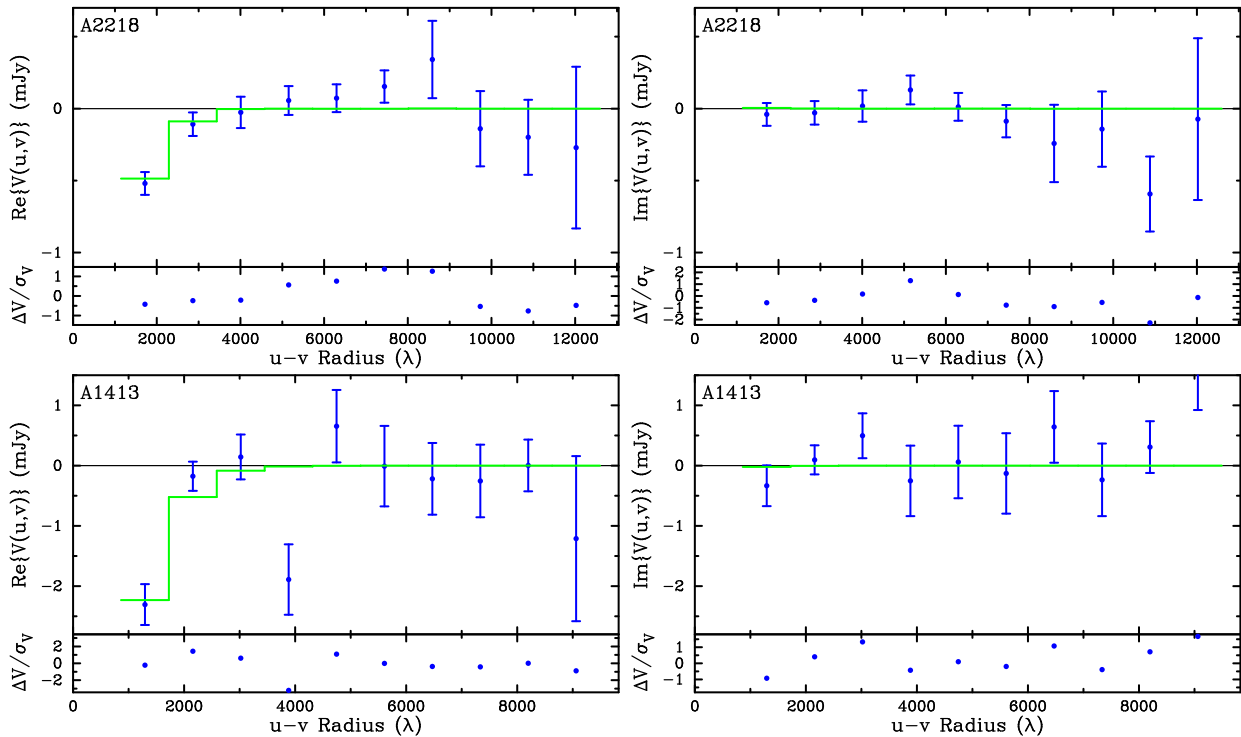


FIG. 5.—Cont.

is shifted to the center of the cluster before azimuthally averaging the real and imaginary components of the complex visibilities. The points with error bars are the data and the best fit model from the joint SZE and X-ray analysis is shown as a solid line, averaged the same way as the data. Also shown are the residuals in units of the standard deviation. A simple χ^2 analysis of the SZE u - v radial profiles reveals that the models provide a good fit to the data for every cluster. The real and imaginary components are shown on the same scale for each cluster for easy comparison, though the scale on the residuals may change. The cluster with the most apparent imaginary component, A520, is also the cluster with its best fit center the furthest away from the pointing center, $\sim 65''$. The primary beam attenuation introduces asymmetry and produces a non-zero imaginary component paralleled in the best fit model for A520.

Figure 6 shows the X-ray radial surface brightness profiles and the best fit composite models for each cluster in the sample. Residuals in units of the standard deviation are also plotted, $\Delta S_x / \sigma_{S_x}$. A simple χ^2 analysis of the radial profiles shows that, in general, the models provide a reasonable fit to the data over a large range of angular radii. There are 3 clusters with residuals $\gtrsim 5 \sigma$ in a few of the radial bins; A1835, A665, and A2281. In A1835 the model systematically underpredicts the surface brightness for a few intermediate radial bins. This cluster contains a strong cooling flow (e.g., Peres et al. 1998), though shows no sign of a central emission excess over the best fit model. The other cooling flow clusters in our sample (see §6.1) do not exhibit large residuals in the X-ray model fit. Both A665 (Gómez et al. 2000; Kaloglyan et al. 1990; Geller & Beers 1982) and A2218 (Cannon et al. 1999; Girardi et al. 1997; Markevitch 1997; Kneib et al. 1995) exhibit complicated structure, possibly indicating a recent merger. Though the worst cases, the best fit models for these 3 clusters still provide reasonable descriptions of the data. The only cluster that shows a marginally significant central X-ray surface brightness excess is A2218, which has not been identified with a cooling flow. We also note that the cooling flow clusters in our sample do not exhibit the largest residuals.

5. DISTANCES AND THE HUBBLE CONSTANT

We use the results from the maximum likelihood model fitting described in §4.2 and §4.3 to compute the angular diameter distance to each of our 18 galaxy clusters. Table 7 shows the derived angular diameter distances for each galaxy cluster as well as the best fit ICM shape parameters. The uncertainties on D_A include the entire observational uncertainty budget, which are shown for each cluster in Table 8. The uncertainties in the fitted parameters come from the procedure described in §4.2.1.

The only other parameter that enters directly into the D_A calculation is T_{e0} . Since $D_A \propto T_{e0}^{-2}$, the uncertainty in D_A due to T_{e0} is listed as twice the fractional uncertainty on T_{e0} . The other parameters, column density and metallicity, as well as T_{e0} , affect the X-ray cooling function. We estimate the uncertainties in D_A due to these parameters by taking their 68.3% ranges and seeing how much they affect the cooling function. The uncertainty on D_A due to observations is dominated by the uncertainty in the electron temperature and the SZE central decrement. Note that changes of factors of two in metallicity result in a $\sim 1\%$ effect on D_A .

The column densities measured from the X-ray spectra are different from those from H I surveys (Dickey & Lockman

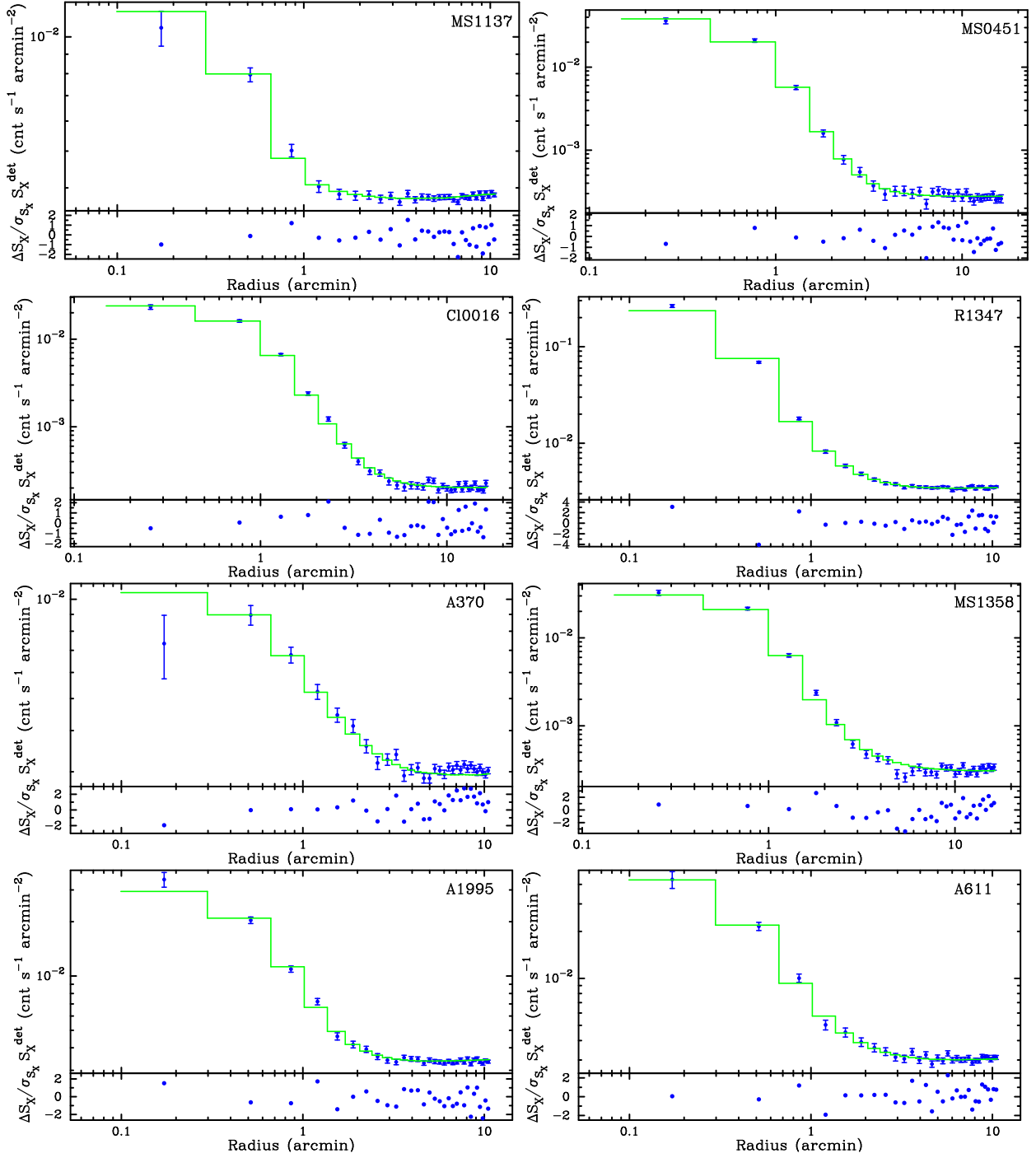


FIG. 6.—X-ray surface brightness radial profiles with the best fit model and residuals in units of the standard deviation. In general, the models provide good fits to the data over a large range of radii.

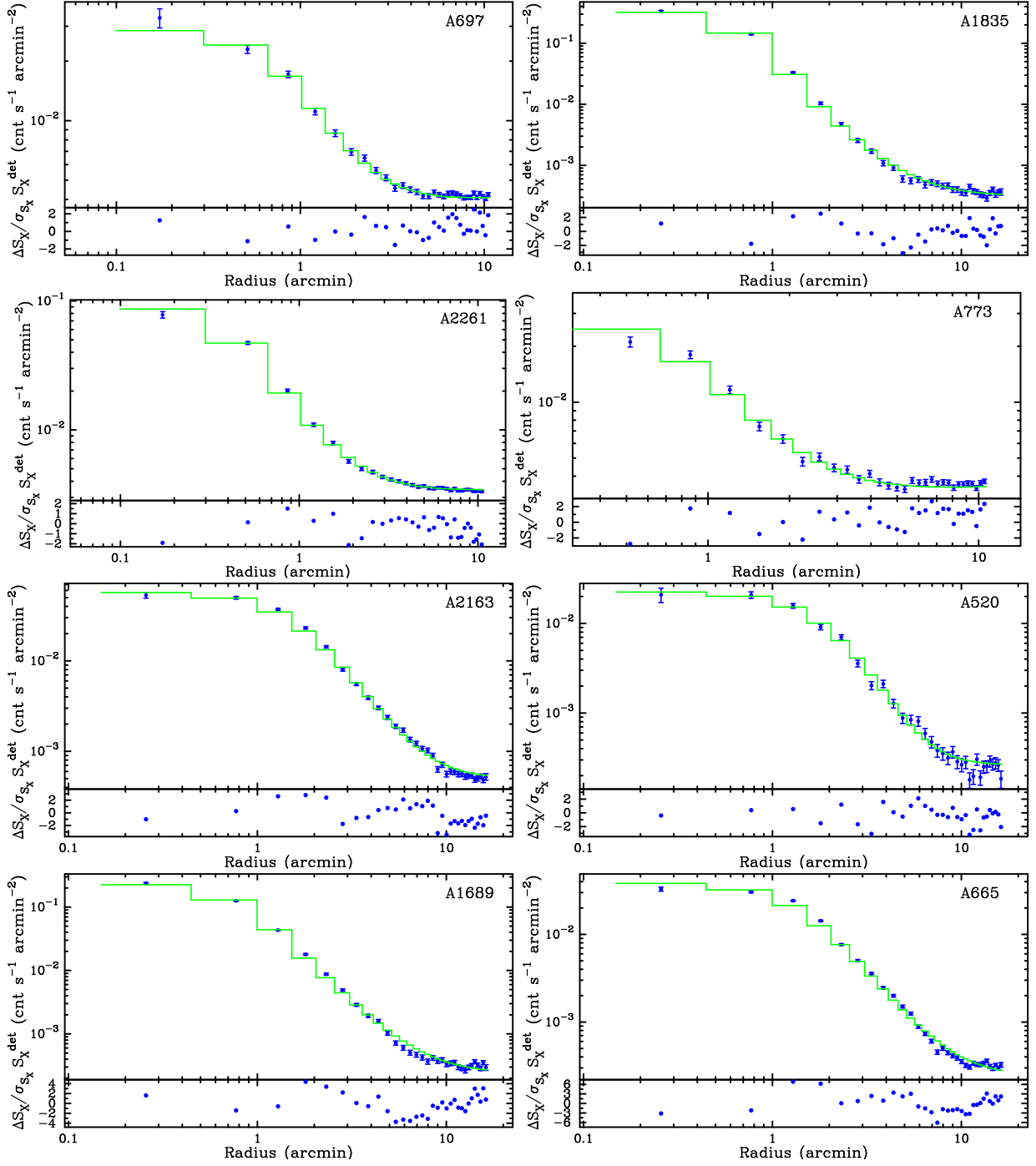


FIG. 6.—Cont.

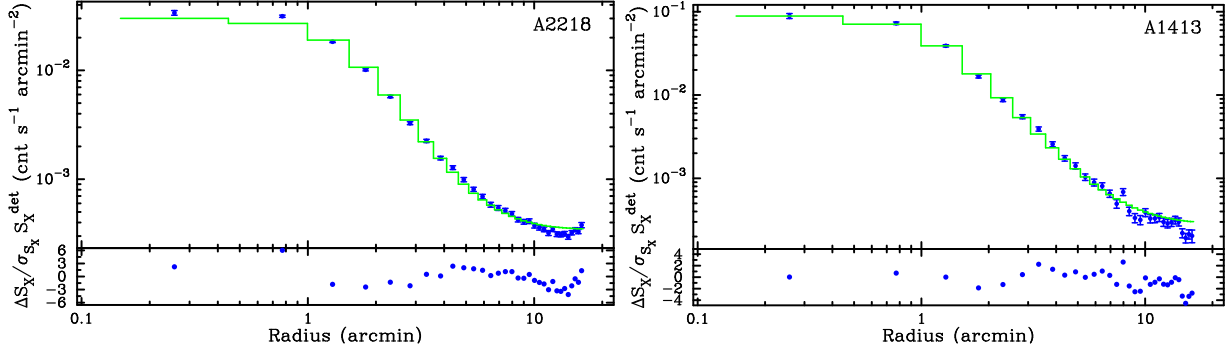


FIG. 6.—Cont.

TABLE 8
 D_A OBSERVATIONAL UNCERTAINTY BUDGET (PERCENT)

Cluster	Fit ^a	T_e ^b	$\Lambda_{eH}(Z)$ ^c	$\Lambda_{eH}(N_H)$ ^b	$\Lambda_{eH}(T_e)$	pt src ^d	Total ^e
MS1137	+22.3	+24.6	+4.9	+ 9.0	+0.0	+ 0.0	+34.7
	-22.9	-45.6	-4.7	- 6.1	-0.8	- 0.0	-51.6
MS0451	+13.8	+15.4	+1.0	+ 0.9	+0.4	+ 0.6	+20.7
	-13.1	-19.2	-1.0	- 1.2	-0.5	- 0.6	-23.4
CL0016	+17.8	+15.4	+1.9	+ 1.1	+0.1	+ 1.0	+23.7
	-16.4	-19.1	-1.2	- 1.2	-0.2	- 0.6	-25.2
R1347	+19.2	+12.9	+1.0	+15.7	+0.4	+11.2	+30.1
	-17.1	-15.1	-1.0	-11.7	-0.5	-11.4	-28.1
A370	+24.4	+15.2	+1.9	+13.1	+0.4	+ 4.0	+31.9
	-16.7	-21.2	-1.9	- 8.2	-0.6	- 4.0	-28.6
MS1358	+24.0	+11.2	+1.5	+ 3.1	+0.3	+10.0	+28.6
	-21.3	-13.4	-1.5	- 3.0	-0.4	-25.2	-35.8
A1995	+10.3	+15.6	+1.1	+ 8.5	+0.5	+ 8.2	+22.1
	-11.5	-20.0	-1.1	- 6.5	-0.7	- 7.8	-25.2
A611	+22.2	+18.2	+3.7	+15.3	+0.4	+ 0.0	+32.7
	-20.5	-18.2	-3.7	- 9.8	-0.5	- 0.0	-29.4
A697	+22.7	+14.3	+3.0	+12.9	+0.7	+ 0.0	+29.9
	-18.7	-14.3	-3.0	- 8.2	-0.7	- 0.0	-25.1
A1835	+13.2	+ 4.1	+0.7	+ 3.7	+0.2	+12.4	+18.9
	-12.6	- 4.6	-0.5	- 3.5	-0.2	-13.4	-19.3
A2261	+25.0	+ 7.3	+0.9	+12.7	+0.4	+ 3.4	+29.2
	-22.9	- 8.4	-0.8	- 8.1	-0.5	- 3.4	-25.9
A773	+21.8	+ 7.8	+0.7	+ 9.3	+0.5	+ 0.0	+24.9
	-20.2	- 8.8	-0.7	- 6.2	-0.5	- 0.0	-22.9
A2163	+16.3	+11.5	+1.2	+ 2.9	+0.7	+ 8.4	+21.8
	-14.4	-18.0	-1.1	- 2.2	-1.0	- 8.6	-24.8
A520	+32.4	+ 9.6	+1.0	+12.1	+0.3	+10.2	+37.3
	-27.2	-11.0	-1.0	-10.2	-0.4	-10.2	-32.7
A1689	+14.4	+ 4.1	+0.5	+ 2.9	+0.2	+19.8	+25.0
	-12.2	- 4.6	-0.5	- 2.8	-0.2	-19.6	-23.7
A665	+45.5	+ 6.9	+0.6	+ 6.7	+0.3	+ 0.4	+46.5
	-37.3	- 7.8	-0.8	- 6.1	-0.4	- 0.6	-38.5
A2218	+30.3	+ 6.0	+0.7	+ 5.2	+0.2	+ 10.0	+32.9
	-31.7	- 6.2	-0.7	- 4.8	-0.2	-10.0	-34.2
A1413	+28.5	+ 4.2	+0.5	+ 3.5	+0.2	+ 7.2	+29.9
	-24.8	- 4.5	-0.5	- 3.3	-0.2	- 7.2	-26.4

^aThe 68.3% uncertainties over the four-dimensional error surface for β , θ_c , S_{x0} , and ΔT_0 .

^b D_A decreases as parameter increases.

^cMetallicity relative to solar.

^dMaximum effect from detected point sources.

^eCombined in quadrature.

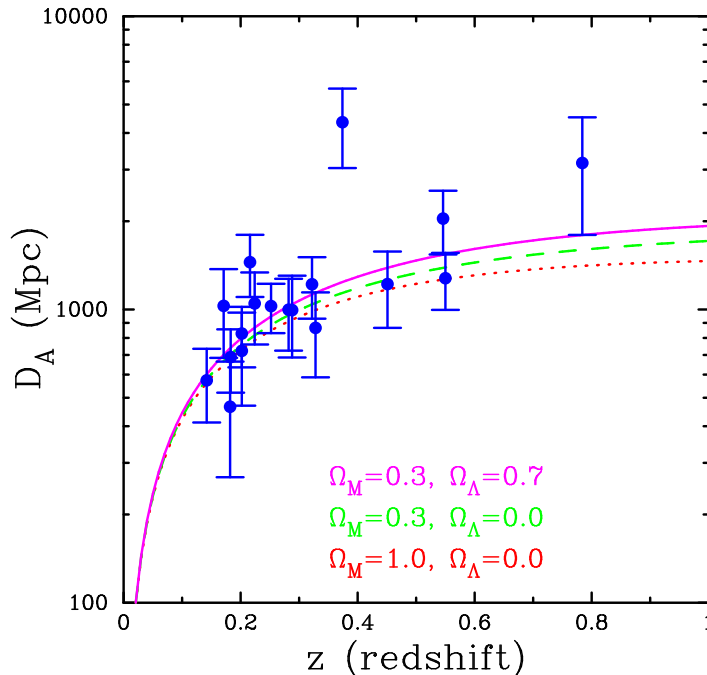


FIG. 7.—SZE determined distances as a function of redshift. The error bars are 68.3% statistical uncertainties only. Also plotted are the theoretical angular diameter distance relations assuming $H_0 = 60 \text{ km s}^{-1} \text{ Mpc}^{-1}$ for three different cosmological models; the currently favored Λ cosmology $\Omega_M = 0.3$, $\Omega_\Lambda = 0.7$ (solid) cosmology; an open $\Omega_M = 0.3$ (dashed) universe; and a flat $\Omega_M = 1$ (dotted) cosmology.

1990). We use the column densities from X-ray spectral fits when possible since that includes contributions from non-neutral hydrogen and other elements which absorb X-rays. For MS0451 and Cl0016, using the survey derived column densities instead of the fitted values changes the angular diameter distance by $\sim \pm 5\%$ (Reese et al. 2000), which we include as a systematic uncertainty (see § 7).

Figure 7 shows the SZE determined distances for each cluster as a function of redshift. Also plotted are the theoretical angular diameter distance relations assuming $H_0 = 60 \text{ km s}^{-1} \text{ Mpc}^{-1}$ for three different cosmologies: the currently favored Λ cosmology $\Omega_M = 0.3$, $\Omega_\Lambda = 0.7$ (solid) cosmology; an open $\Omega_M = 0.3$ (dashed) universe; and a flat $\Omega_M = 1$ (dotted) cosmology. The SZE distances are beginning to probe the angular diameter distance relation. The uncertainties on D_A in Figure 7 are the 68.3% statistical uncertainties only, including all of the statistical uncertainties in the calculation outlined above. We refer the reader to Carroll et al. (1992), Kolb & Turner (1990), and Peacock (1999) for derivations of the theoretical angular diameter distance relation.

There is a known correlation between the β and θ_c parameters of the β model. Figure 8 illustrates this correlation and its effect on D_A for MS1358, and A2261. The filled contours are the 1, 2, and 3 σ ΔS confidence regions for β and θ_c jointly with the plus marking the best fit for each cluster. The lines are contours of constant D_A in megaparsecs. With our interferometric SZE data, the contours of constant D_A lie roughly parallel to the β - θ_c correlation, minimizing the effect of this correlation on the uncertainties of D_A . Similar figures for MS0451 and Cl0016 appear in Reese et al. (2000), which show similar behavior. The alignment of the D_A contours with the β - θ_c correlation is a general feature of our observing strategy. Different observing techniques will result in different behavior. Contours of constant D_A have been found to be roughly orthogonal to this β - θ_c correlation for some single dish SZE observations (Birkinshaw & Hughes 1994; Birkinshaw et al. 1991).

To determine the Hubble Constant, we perform a χ^2 fit to our calculated D_A 's versus z for three different cosmologies. To estimate statistical uncertainties, we combine the uncertainties on D_A listed in Table 8 in quadrature, which is only strictly valid for Gaussian distributions. This combined statistical uncertainty is symmetrized (averaged) and used in the fit. We find

$$H_0 = \begin{cases} 60_{-4}^{+4} \text{ km s}^{-1} \text{ Mpc}^{-1}; & \Omega_M=0.3, \Omega_\Lambda=0.7, \\ 56_{-4}^{+4} \text{ km s}^{-1} \text{ Mpc}^{-1}; & \Omega_M=0.3, \Omega_\Lambda=0.0, \\ 54_{-3}^{+4} \text{ km s}^{-1} \text{ Mpc}^{-1}; & \Omega_M=1.0, \Omega_\Lambda=0.0, \end{cases} \quad (8)$$

where the uncertainties are statistical only at 68.3% confidence. The statistical error comes from the χ^2 analysis and includes uncertainties from T_e , the parameter fitting, metallicity, N_H , and detected radio point sources (see Table 8). We have chosen three cosmologies encompassing the currently favored models. With this sample of clusters, there is a $\sim 10\%$ range in our inferred H_0 due to the geometry of the universe. For the Λ cosmology, $\chi^2 = 16.5$ with a corresponding reduced chi-squared of $\chi_{red}^2 = 0.97$. The difference in χ^2 between the $\Omega_M = 0.3, \Omega_\Lambda = 0.7$ and the flat $\Omega_M = 1$ universes

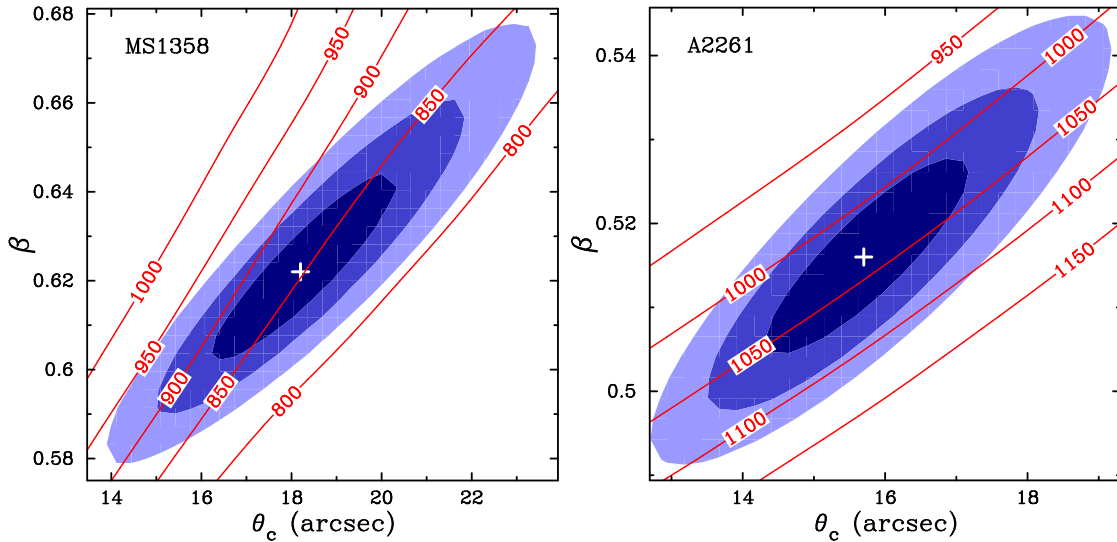


FIG. 8.—Confidence regions from the joint SZE and X-ray fit for MS1358 and A2261. The filled regions are 1, 2, and 3 σ confidence regions for β and θ_c jointly ($\Delta S = 2.3, 6.2, 11.8$), and the cross marks the best-fit β and θ_c . Solid lines are contours of angular diameter distance in megaparsecs. The D_A contours lie roughly parallel to the β - θ_c correlation, minimizing the effect of this correlation on the uncertainties of D_A .

is roughly $\Delta\chi^2 \sim 0.3$, with the Λ cosmology having the lowest χ^2 . Clearly a larger sample of high redshift ($z \sim 1$) clusters is required for a determination of the geometry of the universe from SZE and X-ray determined direct distances to galaxy clusters (see §7).

6. SOURCES OF POSSIBLE SYSTEMATIC UNCERTAINTY

The absolute calibration of both the SZE observations and the PSPC and HRI directly affects the distance determinations. The absolute calibration of the interferometric observations is conservatively known to about 4% at 68.3% confidence, corresponding to a 8% uncertainty in H_0 ($\propto \Delta T_0^{-2}$). The effective areas of the PSPC and HRI are thought to be known to about 10%, introducing a 10% uncertainty into the H_0 determination through the calculation of Σ . In addition to the absolute calibration uncertainty from the observations, there are possible sources of systematic uncertainty

TABLE 9
 H_0 SYSTEMATIC UNCERTAINTY BUDGET (%)

Systematic	Effect
SZE calibration	± 8
X-ray calibration	± 10
N_H	± 5
Asphericity ^a	± 5
Isothermality	± 10
Clumping	-20
Undetected radio sources ^b	± 12
Kinetic SZE ^a	± 2
Primary CMB ^a	$< \pm 1$
Radio Halos	- 3
Primary Beam	± 3
Total ^c	+22 -30

^aIncludes a $1/\sqrt{18}$ factor for our 18 cluster sample.

^bAverage of effect from the 18 cluster fields.

^cCombined in quadrature.

that depend on the physical state of the ICM and other sources that can contaminate the cluster SZE emission. Table 9 summarizes the systematic uncertainties in the Hubble constant determined from our 18 cluster sample.

6.1. Cluster Atmospheres and Morphology

6.1.1. Asphericity

Most clusters do not appear circular in radio, X-rays, or optical. Fitting a projected elliptical isothermal β model gives typical axial ratios that are close to the local average of 0.80 (Mohr et al. 1995). Under the assumption of axisymmetric clusters, the combined effect of cluster asphericity and its orientation on the sky conspires to introduce a $\sim \pm 20\%$ random uncertainty in H_0 determined from one galaxy cluster (Hughes & Birkinshaw 1998). When one considers a large, unbiased sample of clusters, with random orientations, the errors due to imposing a spherical model are expected to cancel, resulting in a precise determination of H_0 . Recently, Sulkanen (1999) studied projection effects using triaxial β models. Fitting these with spherical models he found that the Hubble constant estimated from the sample was within 5% of the input value. We are in the process of using N-body and smoothed particle hydrodynamics (SPH) simulations of 48 clusters to quantify the effects of complex cluster structure on our results.

A 20% effect from one cluster implies a 5% ($= 20/\sqrt{18}$) effect for a sample of 18 clusters. Therefore, we include a 5% effect from asphericity for our cluster sample.

6.1.2. Temperature Gradients

Departures from isothermality in the cluster atmosphere may result in a large error in the distance determination from an isothermal analysis; moreover, an isothermal analysis of a large cluster sample could lead to systematic errors in the derived Hubble parameter if most clusters have similar departures from isothermality (Birkinshaw & Hughes 1994; Inagaki et al. 1995; Holzapfel et al. 1997b). The *ROSAT* band is fairly insensitive to temperature variations, showing a $\sim 10\%$ change in the PSPC count rate for a factor of 2 change in temperature for $T_e > 1.5$ keV gas (Mohr et al. 1999). In theory, cluster temperature profiles may significantly affect the distance determinations through the SZE since $\Delta T \propto \int n_e T_e dl$. The spatial filtering of the interferometer makes our SZE observations insensitive to angular scales larger than a few arcminutes. Therefore we are relatively insensitive to large scale temperature gradients. However, we are sensitive to temperature gradients on smaller scales, for example at the center of cooling flow clusters.

A mixture of simulations and studies of nearby clusters suggests a 10% effect on the Hubble parameter (Inagaki et al. 1995; Roettiger et al. 1997) due to departures from isothermality. The spatial filtering of the interferometer is not accounted for in these studies and thus provides a conservative estimate. We include a conservative $\pm 10\%$ effect on the inferred Hubble parameter due to departures of isothermality, consistent with both cooling flow (see §6.1.3) and non-cooling flow departures.

6.1.3. Cooling Flows

Cooling flows affect the emission weighted mean temperature and enhance the X-ray central surface brightness (see, e.g., Fabian 1994; Nagai et al. 2000). When the cooling time at the center of the cluster is less than the age of the cluster, then the central gas has time to cool. This is known as a cooling flow (e.g., Fabian 1994). The cluster temperature is expected to decrease towards the center of the cluster, which has recently been seen with both Chandra (e.g., Markevitch et al. 2000; Nevalainen et al. 2000) and XMM-Newton (e.g., Tamura et al. 2001).

A characteristic cooling time for the ICM is the available radiative energy divided by its luminosity given by

$$t_{cool} \sim \frac{3kT_e n_{tot}}{2\Lambda n_e n_H} = \frac{3kT_e \mu_H}{2\Lambda n_e \mu_{tot}}, \quad (9)$$

where Λ is the bolometric cooling function of the cluster and all quantities are evaluated at the center of the cluster. Cooling flows may occur if the cooling time is less than the age of the cluster, which we conservatively estimate to be the age of the universe at the redshift of observation, $t_{cool} < t_H(z)$.

As a check, we calculate t_{cool}/t_H ratios for each cluster analyzed by Mohr et al. (1999). We check our cooling flow and non-cooling flow determinations versus those of Peres et al. (1998) and Fabian (1994). Of the 45 clusters in the Mohr sample, 41 have published mass deposition rates. We assume the cluster does not contain a cooling flow if its mass deposition rate is consistent with zero, otherwise it is designated as a cooling flow cluster. We are able to predict whether a cluster has a cooling flow or not with a 90% success rate, suggesting that the ratio t_{cool}/t_H presented in equation (9) is a good predictor for the presence of a cooling flow.

The ratio $t_{cool}/t_H(z)$ for each cluster is summarized in Table 10 for the same three cosmologies used to determine the Hubble constant. The central densities, n_{e0} , used in this calculation are determined by eliminating D_A in equations (2) and (4) in favor of n_{e0} . From this analysis, the seven clusters R1347, MS1358, A611, A1835, A2261, A1689, and A1413 are cooling flow clusters. Both A1995 and A1413 are borderline cases. Such clusters are expected to have falling temperatures towards the center of the cluster.

In principle, the multiphase medium expected in cooling flow clusters could introduce large biases in isothermal beta model SZE and X-ray distances (Nagai & Mohr 2002). However, recent observations with Chandra and XMM-Newton suggest that cooling flows are not as strong as previously expected (e.g., Fabian et al. 2001; Peterson et al. 2001). To estimate the possible effects of cooling flow-like temperature profiles, we adopt the deprojected temperature profile of A1835

from an analysis of XMM-Newton observations and determine the change in the angular diameter distance introduced by this profile. The inclusion of the A1835 temperature profile reduces the angular diameter distance by $\sim 10\%$, causing a $\sim 10\%$ underestimate in the Hubble constant from cooling flow clusters when an isothermal analysis is performed (A. D. Miller 2001, private communication). In addition, a theoretical examination of the effects of cooling flows on SZE and X-ray determined distances suggests a $\sim 10\%$ underestimate of H_0 from an isothermal analysis (Majumdar & Nath 2000). Assuming all seven cooling flow clusters in our sample produce a similar 10% bias in H_0 , the average underestimate in H_0 for our 18 cluster sample is $\sim 4\%$.

We combine the uncertainty from cooling flow and non-cooling flow (see §6.1.2) departures from isothermality into a conservative $\pm 10\%$ effect on the inferred Hubble parameter.

6.1.4. Clumping; Small Scale Structure

Clumping of the intracluster gas is a potentially serious source of systematic error in the determination of the Hubble constant. Unresolved clumps in an isothermal intracluster plasma will enhance the X-ray emission by the factor

$$C \equiv \frac{\langle n_e^2 \rangle}{\langle n_e \rangle^2}. \quad (10)$$

The cluster generates more X-ray emission than expected from a uniform ICM leading to an underestimate of the angular diameter distance ($D_A \propto S_x^{-1}$) and therefore an overestimate of the Hubble parameter for $C > 1$. Unlike the orientation bias which averages down for a large sample of clusters, clumping must be measured in each cluster or estimated for an average cluster. Theoretical estimates of C are difficult because they must account for the complicated processes that both generate and damp density enhancements, such as preheating and gas-dynamical processes.

There is currently no observational evidence of significant clumping in galaxy clusters. If clumping were significant and had large variations from cluster to cluster, we might expect larger scatter than is seen in the Hubble diagrams from SZE and X-ray distances (Figure 7; see also Birkinshaw 1999). Gas-dynamical cluster simulations provide an opportunity to test the effects of observing strategy and cluster structure on our distance determinations. These simulated clusters exhibit X-ray merger signatures consistent with those observed in real clusters and, presumably, they exhibit the appropriate complexities in their temperature structure as well. Preliminary work indicates that temperature profiles do not introduce a large error on our distances but that clumping in the ICM may bias distances low by up to $\sim 20\%$. As mentioned above, there is no observational evidence of clumping within the ICM. However, merger signatures are common (Mohr et al. 1995), and the mergers are the driving mechanism behind these fluctuations in the simulated clusters (Mathiesen et al. 1999).

Clumping causes an overestimate of H_0 , so we include a conservative one-sided -20% possible systematic due to clumping.

TABLE 10
RATIO OF $t_{cool}/t_H(z)$

Cluster	Cosmology (Ω_M, Ω_Λ)		
	(0.3, 0.7)	(0.3, 0.0)	(1.0, 0.0)
MS1137	1.1	1.9	1.4
MS0451	1.0	1.6	1.2
Cl0016	1.5	2.5	1.9
R1347	0.1	0.2	0.1
A370	3.6	5.8	4.4
MS1358	0.4	0.7	0.5
A1995	0.9	1.5	1.2
A611	0.4	0.7	0.5
A697	1.1	1.7	1.3
A1835	0.1	0.2	0.2
A2261	0.3	0.5	0.4
A773	1.5	2.4	1.8
A2163	1.3	2.0	1.6
A520	2.1	3.3	2.6
A1689	0.3	0.5	0.4
A665	1.2	1.8	1.4
A2218	1.4	2.2	1.7
A1413	0.6	0.9	0.7

6.2. Possible SZE Contaminants

6.2.1. Possible Undetected Point Sources in the Field

Undetected point sources near the cluster center mask the central decrement, causing an underestimate in the magnitude of the decrement and therefore an underestimate of the angular diameter distance. The synthesized beam shapes, which include negative sidelobes, allow both underestimates and overestimates in the magnitude of the decrement. As a conservative estimate of our detection threshold, we use 3 times the rms of the high resolution map, applying a $\geq 2000 \lambda$ cut on the baselines for each cluster data set. Placing a point source with flux equal to our detection limit near the cluster center and re-analyzing to find the change in the central decrement provides an estimate of the upper bound of the effects of undetected radio point sources.

We have additional information on the distribution of point sources in all our cluster fields from observations at lower frequencies. Sources with flux densities greater than 2 mJy at 1.4 GHz appear in the NVSS catalog (Condon et al. 1998). We use the NVSS catalog to find point sources within $400''$ of each cluster center. We extrapolate the NVSS sources in our fields to 28.5 GHz using the average spectral index of radio sources in galaxy clusters $\alpha = 0.77$ (Cooray et al. 1998), where $S_\nu \propto \nu^{-\alpha}$. Extrapolated NVSS sources with fluxes greater than our 3σ threshold are ruled out by the 30 GHz data and their fluxes are fixed at the maximal 30 GHz 3σ value. The extrapolated NVSS sources are added to the 30 GHz visibilities data, which is re-analyzed, not accounting for the additional point sources. The uncertainty on the angular diameter distance from undetected point sources is summarized in Table 11 for each cluster field. The average over the 18 cluster fields yields a $\sim 12\%$ uncertainty on the Hubble parameter.

We know that clusters have central dominant (cD) galaxies, which are often radio bright. Therefore it is likely that there is a radio point source near the center of each cluster. To estimate the effects of cD galaxies on the central decrement we pick three clusters for which we do not detect a central radio point source, A697, A2261, and A1413. We add a point source fixed at the optical position of the cD (Crawford et al. 1999) and vary both the flux of the cD galaxy and the central decrement, keeping the ICM shape parameters fixed at their best-fit values. The cD fluxes are all consistent with zero and the corresponding changes in the central decrement are $\lesssim 2\%$. This suggests that undetected cD galaxies do not contribute significantly to the uncertainty on the Hubble constant, $\lesssim 4\%$, within our uncertainty budget for possible undetected point sources.

TABLE 11
EFFECTS OF UNDETECTED POINT SOURCES ON D_A (%)

Cluster	Effect (%)
MS1137	0
MS0451	0
CL0016	2
R1347 ^a	32
A370	6
MS1358 ^b	0
A1995	6
A611 ^b	0
A697	6
A1835	0
A2261 ^a	46
A773	6
A2163 ^a	22
A520 ^a	16
A1689 ^a	18
A665 ^a	12
A2218	0
A1413	42
Average	12

^aRequired 30 GHz 3σ truncation.

^bNo NVSS sources in the cluster field.

6.2.2. Kinetic SZE

Cluster peculiar velocities with respect to the CMB introduce an additional CMB spectral distortion known as the kinetic SZE. The kinetic SZE is proportional to the thermal effect but has a different spectral signature so it can be distinguished from the thermal SZE with spectral SZE observations. For a 10 keV cluster with a line-of-sight peculiar velocity of 1000 km s^{-1} , the kinetic SZE is $\sim 11\%$ of the thermal SZE at 30 GHz. Watkins (1997) presented observational evidence suggesting a one-dimensional rms peculiar velocity of $\sim 300 \text{ km s}^{-1}$ for clusters, and recent simulations found similar results (Colberg et al. 2000). With a line-of-sight peculiar velocity of 300 km s^{-1} and a more typical 8 keV cluster, the kinetic SZE is $\sim 4\%$ of the thermal effect, introducing up to a $\sim \pm 8\%$ correction to the angular diameter distance computed from one cluster. When averaged over an ensemble of clusters, the effect from peculiar velocities should cancel, manifesting itself as an additional statistical uncertainty similar to the effects of asphericity. Therefore, we include a 2% ($= 8/\sqrt{18}$) effect from the kinetic SZE for our 18 cluster sample.

6.2.3. CMB Primary Anisotropies

CMB primary anisotropies have the same spectral signature as the kinetic SZE. Recent BIMA observations provide limits on primary anisotropies on the scales of the observations presented here (Dawson et al. 2001; Holzapfel et al. 2000). They place a 95% confidence upper limit to the primary CMB anisotropies of $\Delta T < 19 \mu\text{K}$ at $\ell \sim 5500$ ($\sim 2'$ scales). Thus primary CMB anisotropies are an unimportant ($\lesssim 2\%$) source of uncertainty for our observations. At 68.3% confidence, primary CMB anisotropies contribute a $\lesssim 1\%$ uncertainty in the measured Hubble parameter. In addition, CMB primary anisotropy effects on the inferred H_0 should average out over the sample; with an 18 cluster sample CMB primary anisotropy contributes $< 1\%$ uncertainty to H_0 .

6.2.4. Radio Halos

The SZE decrement may be masked by large scale diffuse non-thermal radio emission in clusters of galaxies, known as radio halos. If present, radio halos are located at the cluster centers, have sizes typical of galaxy clusters, and a steep radio spectrum $\alpha \sim 1 - 3$ (Kempner & Sarazin 2001; Giovannini et al. 1999; Moffet & Birkinshaw 1989; Hanisch 1982). Similar structures at the cluster periphery, usually with an irregular shape, are called relics. In general, radio halos and relics are rare phenomena that are present in rich, massive clusters, characterized by high X-ray luminosity and high temperature (Giovannini & Feretti 2000; Giovannini et al. 1999). Cooling flow clusters rarely contain radio halos. Because halos and relics are rare, little is known about their nature and origin but they are thought to be produced by synchrotron emission from an accelerated or reaccelerated population of relativistic electrons (e.g., Jaffe 1977; Dennison 1980; Roland 1981; Schlickeiser et al. 1987). Shocks from cluster mergers may be the acceleration mechanism though there are numerous theories (e.g., Jaffe 1977, 1980; Dennison 1980; Roland 1981; Schlickeiser et al. 1987; Ensslin et al. 1998; Blasi & Colafrancesco 1999; Dolag & Ensslin 2000; Liang et al. 2000).

According to the literature (Kempner & Sarazin 2001; Giovannini & Feretti 2000; Giovannini et al. 1999), the following clusters in our sample exhibit radio halos: Cl0016, A773, A2163, A520, A665, A2218. In Figure 9, we show NVSS 1.4 GHz image contours (Condon et al. 1998) overlaid on color scale images of the SZE cluster emission. Contours are multiples of twice the rms in the NVSS maps ($\text{rms} \sim 0.45 \text{ mJy beam}^{-1}$). It is apparent that many of these halos are at the $2\sigma \approx 0.9 \text{ mJy beam}^{-1}$ level. The brightest known halo is seen in A2163 with a peak brightness of $\sim 5.4 \text{ mJy beam}^{-1}$.

For each of the halo clusters, we conservatively model the halo as a point source at the cluster center with flux from an $\alpha = 1$ extrapolation of the peak NVSS halo flux and re-analyze to determine the effect on the central decrement. The average effect on the central decrement from the clusters with radio halos in our sample is 4%, excluding A2163 which shows a $\sim 10\%$ effect on the central decrement. Radio halos typically have spectral indices $\alpha \geq 1.5$, making the $\alpha = 1$ extrapolation a conservative upper bound for the effects of radio halos. Averaged over the entire 18 cluster sample, the $\alpha = 1$ extrapolation results imply a $\sim 3\%$ overestimate (-3% effect) on our inferred Hubble parameter ($H_0 \propto \Delta T^{-2}$) from radio halos.

6.2.5. Imprecisely Measured Primary Beam

The primary beam is determined from holography measurements at both OVRO and BIMA. The effect of the primary beam on the interferometric observations is a convolution in the Fourier plane (see §3.1.1) or equivalently, an attenuation across the field of view. Therefore, differences in primary beam shape simply alter the smoothing kernel in the u - v plane only slightly, having a small affect on the derived distances.

To assess the effects of the primary beam quantitatively, we fit to an OVRO and BIMA data set using a cluster model attenuated by a Gaussian beam with different assumed FWHMs. There is no significant change in the central decrements when using a Gaussian approximation for the primary beam instead of the measured beam. Even with an unrealistically large $\pm 0.2'$ uncertainty in the primary beam FWHM, the uncertainty introduced in the Hubble constant is $\lesssim 3\%$ ($\lesssim 2\%$ in ΔT_0). Artificially broadening the wings of the real beam has a negligible effect on the derived central decrements. We adopt a 3% uncertainty in H_0 as a conservative estimate of the maximum effects from an imprecisely measured primary beam.

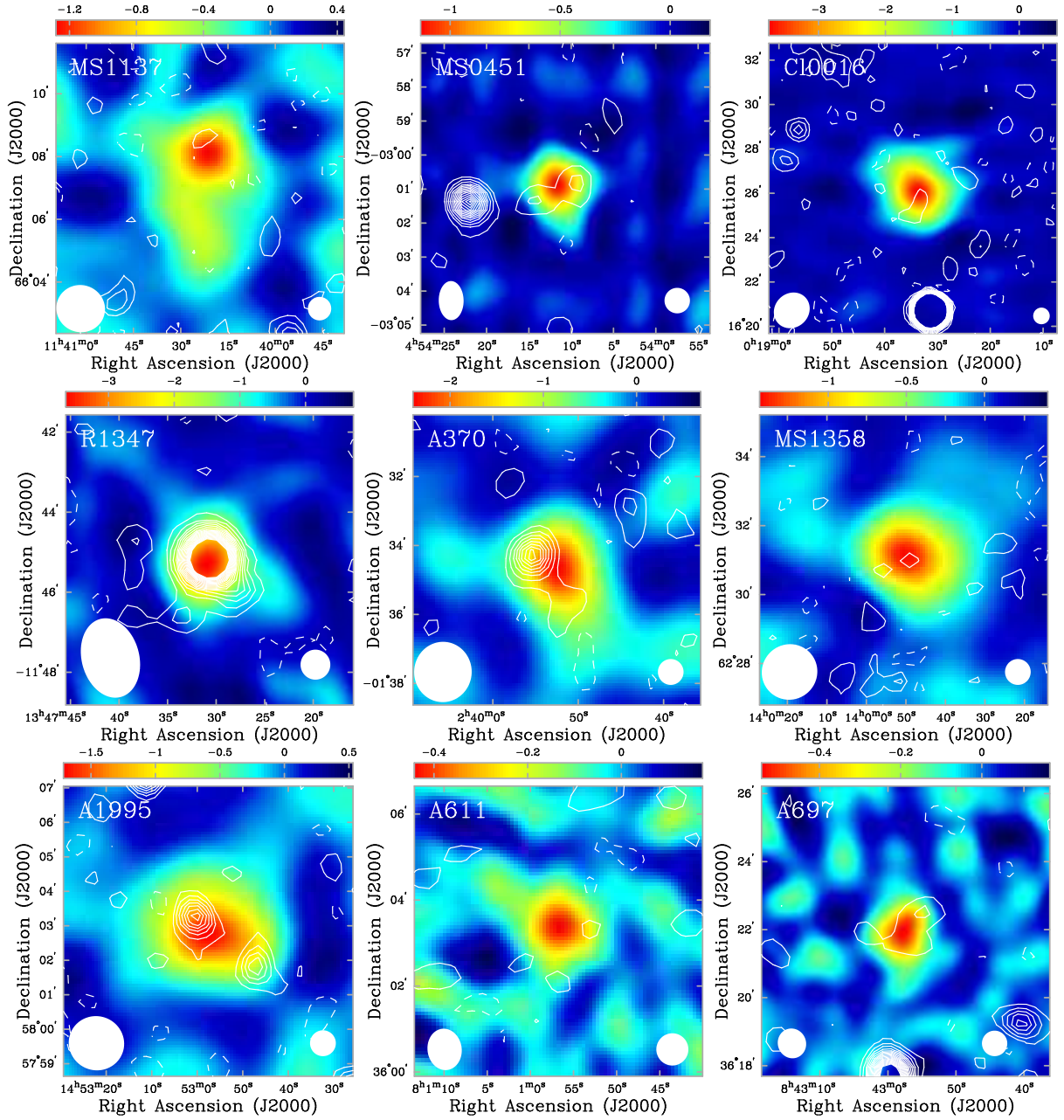


FIG. 9.—SZE from our own 30 GHz observations (color scale) with NVSS 1.4 GHz contours. The 30 GHz images are the color scale version of the SZE shown in Figure 2. The color scale wedge above each image shows the range in the flux density of the 30 GHz map in units of mJy beam^{-1} . Contours are multiples of twice the rms and the NVSS rms is $\sim 0.45 \text{ mJy beam}^{-1}$. The FWHM of the 30 GHz synthesized beam is shown in the lower left hand corner of each panel and the $45''$ FWHM beam of the NVSS survey is shown in the lower right hand corner of each panel. A2163 exhibits the brightest 1.4 GHz radio halo in our 18 cluster sample.

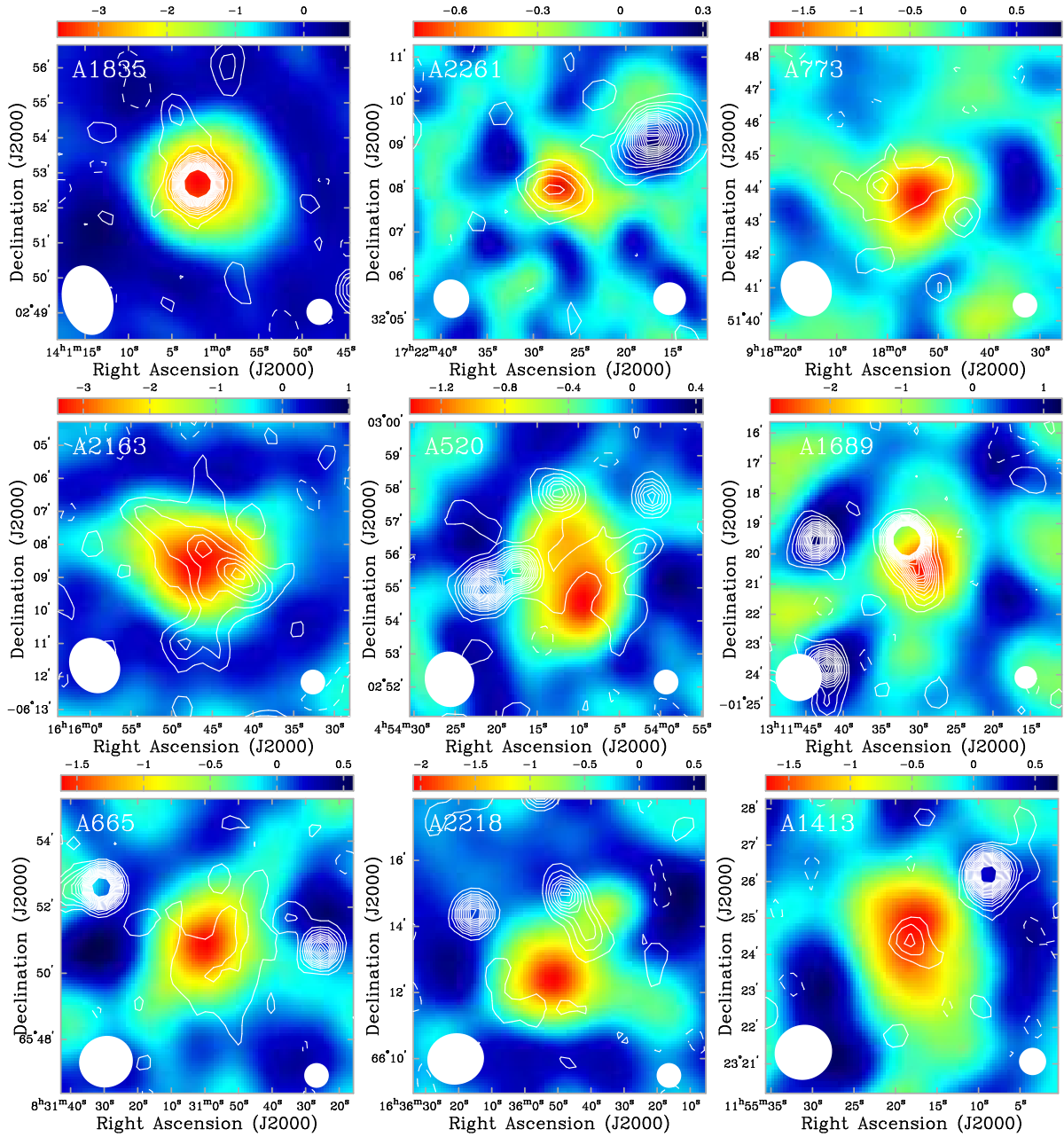


FIG. 9.—Cont.

7. DISCUSSION AND CONCLUSION

We perform a maximum-likelihood joint fit to centimeter-wave interferometric SZE and *ROSAT* X-ray (PSPC and HRI) data to constrain the ICM parameters for a sample of high redshift clusters of galaxies. We model the ICM as a spherical, isothermal β model. From this analysis we determine the distances to 18 galaxy clusters. Together, these distances imply a Hubble constant of

$$H_0 = \begin{cases} 60_{-4}^{+4} {}_{-18}^{+13} \text{ km s}^{-1} \text{ Mpc}^{-1}; & \Omega_M=0.3, \Omega_\Lambda=0.7, \\ 56_{-4}^{+4} {}_{-17}^{+12} \text{ km s}^{-1} \text{ Mpc}^{-1}; & \Omega_M=0.3, \Omega_\Lambda=0.0, \\ 54_{-3}^{+4} {}_{-16}^{+12} \text{ km s}^{-1} \text{ Mpc}^{-1}; & \Omega_M=1.0, \Omega_\Lambda=0.0, \end{cases} \quad (11)$$

where the uncertainties are statistical followed by systematic at 68.3% confidence. The systematic uncertainties have been added in quadrature and include an 8% (4% in ΔT_0) uncertainty from the absolute calibration of the SZE data, a 10% effective area uncertainty for the PSPC and HRI, a 5% uncertainty from the column density, a 5% ($\simeq 20/\sqrt{18}$) uncertainty due to asphericity, a 10% effect for our assumptions of isothermality, a one-sided -20% effect from possible small-scale clumping in the ICM, a 12% uncertainty from undetected radio sources, a 2% ($\simeq 8/\sqrt{18}$) uncertainty from the kinetic SZE, a 1% uncertainty from primary CMB anisotropies, a -3% effect from radio halos, and a 3% effect from an imprecisely measured primary beam. These systematic uncertainties are summarized in Table 9. We adopt conservative assumptions when gauging the effects of possible systematics. The contributions from asphericity, kinetic SZE, and primary CMB are expected to average out for a large sample.

The measured distances plotted in Figure 7 with the theoretical relation show that A370 is the largest outlier from the theoretical angular diameter distance relation and MS1137 has the largest distance uncertainty. A370 exhibits an almost 2-to-1 axial ratio in the knotty N-S elongation of its X-ray image (see Fig 2). An optical study of this cluster and its member galaxies shows that the cluster is dominated by two giant elliptical galaxies with a projected separation of about $40''$, roughly in the north-south direction (Mellier et al. 1988). In addition, gravitational lens models suggest that A370 has a bimodal mass distribution with the two components separated in a roughly north-south direction (Kneib et al. 1993; Soucail et al. 1988; Smail et al. 1996). The spherical model used is clearly insufficient for the complex structure of this cluster. The uncertainties on the distance to MS1137 are particularly large since MS1137 resides in the distant universe ($z = 0.78$), making it difficult to collect large numbers of X-ray photons. Therefore, the uncertainties on the X-ray driven quantities are large; in particular, the uncertainty on the measured X-ray temperature is the main contributor to the large uncertainty on the angular diameter distance to MS1137. The large uncertainties on the distances to both A370 and MS1137 mean that those clusters contribute little weight in the determination of the Hubble constant.

As discussed in §2, target clusters were originally chosen from a limited sample of known X-ray clusters. We construct subsamples of our cluster sample to explore the robustness of our result and to look for possible biases in our H_0 determination. A description of the subsamples, the number of clusters in each subsample N , the Hubble constant from each subsample, and the χ^2 and reduced χ^2 for the Hubble parameter are summarized in Table 12 for each subsample considered. Only the $\Omega_M = 0.3$, $\Omega_\Lambda = 0.7$ cosmology is considered in this study. Other cosmologies will have similar changes to the best fit Hubble parameter. Table 12 shows that excluding the largest outlier, A370, has a negligible effect on the determined Hubble parameter. We also split the sample up based on having a cooling flow, by redshift, presence of a radio halo, based on point sources, based on right ascension and declination, based on X-ray luminosity, and based on membership in the EMSS survey or being an Abell cluster.

Jones et al. (2002) constructed an orientation unbiased sample of galaxy clusters for a SZE and X-ray determination of the Hubble parameter. Most importantly, they drew clusters present in both the BCS (Ebeling et al. 2000a; Crawford et al. 1999; Ebeling et al. 1998, 1997) and NORAS (Böhringer et al. 2000) surveys with $L_x > 8 \times 10^{44} \text{ erg s}^{-1}$ and well above the survey flux limits ($> 5 \times 10^{-12} \text{ erg s}^{-1} \text{ cm}^{-2}$). Eleven clusters satisfy these criterion as well as their redshift range choice ($0.14 \leq z \leq 0.30$) and declination constraint ($\geq 2^\circ$). They find five of the eleven to be sufficiently free from point sources at 15 GHz for SZE measurements. Six of these eleven are part of our sample, which we call our orientation unbiased subsample in Table 12.

All of these subsamples yield a Hubble constant with 1σ statistical uncertainties consistent with the H_0 from the entire 18 cluster sample. This argues in favor of a robust H_0 determination.

We compare our results with other SZE determined distances to clusters in our sample in Table 13. Only statistical uncertainties are included. There are nine clusters in our sample that also have previously determined SZE distances. All of the 1σ confidence regions agree with our own, with the exception of Cl0016, R1347, A773, and A665. The systematic uncertainties on the angular diameter distance are $\gtrsim 30\%$ for one galaxy cluster. Therefore, all of the distances are in reasonably good agreement, even after accounting for shared systematics (namely most use ROSAT X-ray data and ASCA X-ray temperatures).

Many of the systematics can be approached and reduced through improved observations. For example, Chandra and XMM-Newton are now producing temperature profiles of galaxy clusters (e.g., Markevitch et al. 2000; Nevalainen et al. 2000; Tamura et al. 2001). The unprecedented angular resolution of Chandra will provide insight into possible clumping in clusters. The effects of undetected point sources are being addressed with multi-wavelength (5 and 8 GHz) VLA observations of many of our cluster fields. In addition, there is a project to produce a $\sim 1\%$ calibration of the modified OVRO and BIMA SZE systems and the current generation of X-ray satellites will reduce the X-ray absolute calibration uncertainty to the few percent level.

The 18 cluster distances presented here are beginning to probe the shape of the angular diameter distance relation.

TABLE 12
 H_0 FROM DIFFERENT SUBSAMPLES FOR THE Λ COSMOLOGY

Subsample	N	H_0 ($\text{km s}^{-1} \text{Mpc}^{-1}$)	χ^2	χ_{red}^2 ^a
All	18	60^{+4}_{-4}	16.5	0.97
No A370	17	61^{+4}_{-4}	10.8	0.68
No MS1137 or A370	16	61^{+5}_{-4}	9.8	0.65
No cooling flow	11	59^{+6}_{-5}	14.5	1.45
Only cooling flow	7	63^{+7}_{-6}	1.7	0.28
$z > 0.27$	9	62^{+7}_{-6}	9.7	1.21
$z < 0.27$	9	59^{+6}_{-5}	6.6	0.83
No point sources	4	53^{+9}_{-7}	3.4	1.13
Only point sources	14	62^{+5}_{-4}	12.2	0.94
Only radio halo	6	56^{+8}_{-6}	6.7	1.34
No halo	12	62^{+5}_{-5}	9.3	0.85
$\text{RA} < 11.5^{\text{h}}$	9	61^{+7}_{-6}	13.6	1.70
$\text{RA} > 11.5^{\text{h}}$	9	60^{+6}_{-5}	2.9	0.36
$\text{Dec} > 30^\circ$	9	60^{+7}_{-6}	8.3	1.04
$\text{Dec} < 30^\circ$	9	61^{+6}_{-5}	8.1	1.01
$L_x > 14.5 \times 10^{44} \text{ erg s}^{-1}$	9	63^{+6}_{-5}	4.4	0.55
$L_x \leq 14.5 \times 10^{44} \text{ erg s}^{-1}$	9	57^{+7}_{-5}	11.5	1.44
EMSS clusters	5	66^{+10}_{-8}	3.5	0.88
Abell clusters	13	58^{+5}_{-4}	12.2	1.02
Orientation unbiased	6	58^{+8}_{-6}	6.2	1.24

^a $\chi_{red}^2 = \chi^2 / (N - 1)$, where $N - 1$ is the degrees of freedom.

TABLE 13
COMPARISON OF SZE DETERMINED DISTANCES

Cluster	D_A^a (Mpc)	reference
Cl0016	2041 ± 499	This work
	1788 ± 664	H98
	1100 ± 295	G02
R1347	1221 ± 356	This work
	1890 ± 644	P01
	1897 ± 401	K99
A697	998 ± 274	This work
	1044 ± 239	J02
A1835	1027 ± 196	This work
	867 ± 411	M00
A773	1450 ± 347	This work
	1002 ± 257	S99
A2163	828 ± 193	This work
	728 ± 387	H97
	615 ± 327	L98
A665	466 ± 198	This work
	1017 ± 229	B91
A2218	1029 ± 346	This work
	616 ± 118	B94
	720 ± 422	T98
	1201 ± 343	J02
A1413	573 ± 161	This work
	565 ± 164	G02b

^aIncludes approximate 68.3% confidence statistical uncertainties only.

REF: B91-Birkinshaw et al. 1991; B94-Birkinshaw & Hughes 1994; G02-Grainge et al. 2002a; G02b-Grainge et al. 2002b H97-Holzzapfel et al. 1997b; H98-Hughes & Birkinshaw 1998; J02-Jones et al. 2002; K99-Komatsu et al. 1999; L98-Lamarre et al. 1998; M00-Mauskopf et al. 2000; P01-Pointecouteau et al. 2001; S99-Saunders et al. 1999; T98-Tsuboi et al. 1998;

Moreover, constructing subsamples from our 18 cluster sample based on such considerations as cooling flows, redshift, and X-ray luminosity, does not significantly affect the best fit H_0 , suggesting a robust determination of the Hubble parameter. Systematics currently dominate the uncertainty in our determination of the Hubble parameter. These systematics can and will be addressed with current radio observatories (OVRO, BIMA, and VLA) and X-ray satellites (Chandra and XMM-Newton). With a sample of high redshift galaxy clusters, this method can be used to constrain the geometry of the universe, providing a valuable independent check of the recent supernovae type Ia (Schmidt et al. 1998; Riess et al. 1998; Perlmutter et al. 1999; Goobar et al. 2000) and primary CMB power spectrum results (Pryke et al. 2002; de Bernardis et al. 2002; Stompor et al. 2001). We emphasize that SZE and X-ray determined distances are independent of the extragalactic distance ladder and do not rely on clusters being standard candles or rulers.

A complete review of other distance determination methods is beyond the scope of this paper. We will just touch on a few methods that complement SZE determined distances. The SZE derived distances are direct, making them an interesting check of the cosmological distance ladder. Our measurement of H_0 in the distant universe, agrees within the uncertainties with the Hubble Space Telescope (HST) H_0 Key Project results, which probes the nearby universe. The HST H_0 Key Project finds $H_0 = 72 \pm 3 \pm 7 \text{ km s}^{-1} \text{ Mpc}^{-1}$ (Freedman et al. 2001), where the uncertainties are statistical followed by systematic at 68.3% confidence. Though few in number, there are other methods that yield distances that are independent of the extragalactic distance ladder. Recent observations of masers orbiting the nucleus of the nearby galaxy NGC 4258 (Herrnstein et al. 1999) illustrate a method of determining direct distances in the nearby universe. Time delays produced by lensing of QSO's by galaxies are another direct distance indicator that can probe the high-redshift universe (for recent examples, see Fassnacht et al. 1999; Biggs et al. 1999; Lovell et al. 1998; Barkana 1997; Schechter et al. 1997).

SZE surveys provide a promising method of detecting high redshift galaxy clusters (e.g., Holder et al. 2000; Barbosa et al. 1996). These surveys will provide large catalogs of high redshift galaxy clusters required to determine the geometry of the universe from SZE and X-ray determined direct distances.

This work is the thesis work of E. D. R and benefited from useful discussions from very many people. In particular, we thank Gilbert Holder, Jack Hughes, Carlo Graziani, Sandeep Patel, and Thomas Crawford for useful and stimulating discussions. This project would not have been possible without all of the help and support of both the OVRO and BIMA staff over many years. In particular, E. D. R would like to thank D. Woody, S. Scott, R. Lawrence, J. R. Forster (Rick), R. Plambeck (Dick), J. Wirth (Red), M. Warnock, and M. Masters for both helping to keep our observations going and for teaching E. D. R. all about the details of each observatory. Dave, Rick, and Dick have been especially patient teachers. We would also like to thank the staff of the High Energy Astrophysics Science Archive Research Center (HEASARC). They always responded promptly, politely, and informatively to our many inquiries over the past few years. In particular, Michael Corcoran and Michael Arida have received the brunt of our questions and have been most helpful.

This work is supported by NASA LTSA grant NAG5-7986. E. D. R acknowledges support from NASA GSRP Fellowship NGT5-50173 and the NASA Chandra Postdoctoral Fellowship PF1-20020. This research has made use of data obtained through the High Energy Astrophysics Science Archive Research Center Online Service, provided by the NASA/Goddard Space Flight Center. This work has also made use of the online NVSS and FIRST catalogs operated by the NRAO as well as the NASA/IPAC Extragalactic Database (NED), which is operated by the Jet Propulsion Laboratory, California Institute of Technology, under contract with the National Aeronautics and Space Administration.

REFERENCES

- Allen, S. W. 2000, MNRAS, 315, 269
 Allen, S. W. & Fabian, A. C. 1998a, MNRAS, 297, L57
 —. 1998b, MNRAS, 297, L63
 Arnaud, M. & Evrard, A. E. 1999, MNRAS, 305, 631
 Barbosa, D., Bartlett, J. G., Blanchard, A., & Oukbir, J. 1996, A&A, 314, 13
 Barkana, R. 1997, ApJ, 489, 21
 Biggs, A. D., Browne, I. W. A., Helbig, P., Koopmans, L. V. E., Wilkinson, P. N., & Perley, R. A. 1999, MNRAS, 304, 349
 Birkinshaw, M. 1999, Physics Reports, 310, 97
 Birkinshaw, M. & Hughes, J. P. 1994, ApJ, 420, 33
 Birkinshaw, M., Hughes, J. P., & Arnaud, K. A. 1991, ApJ, 379, 466
 Blasi, P. & Colafrancesco, S. 1999, Astroparticle Physics, 12, 169
 Böhringer, H., et al. 2000, ApJS, 129, 435
 Cannon, D. B., Ponman, T. J., & Hobbs, I. S. 1999, MNRAS, 302, 9
 Carlstrom, J. E., Grego, L., Holzappel, W. L., & Joy, M. 1998, Eighteenth Texas Symposium on Relativistic Astrophysics and Cosmology, ed A. Olinto, J. Frieman, and D. Schramm, World Scientific, 261
 Carlstrom, J. E., Joy, M., & Grego, L. 1996, ApJ, 456, L75
 Carlstrom, J. E., Joy, M., Grego, L., Holder, G., Holzappel, W. L., LaRoque, S., Mohr, J. J., & Reese, E. D. 2000, in Constructing the Universe with Clusters of Galaxies, ed. F. Durret & G. Gerbal, IAP
 Carroll, S. M., Press, W. H., & Turner, E. L. 1992, ARA&A, 30, 499
 Cash, W. 1979, ApJ, 228, 939
 Cavaliere, A. & Fusco-Femiano, R. 1976, A&A, 49, 137
 —. 1978, A&A, 70, 677
 Challinor, A. & Lasenby, A. 1998, ApJ, 499, 1
 Colberg, J. M., White, S. D. M., MacFarland, T. J., Jenkins, A., Pearce, F. R., Frenk, C. S., Thomas, P. A., & Couchman, H. M. P. 2000, MNRAS, 313, 229
 Condon, J. J., Cotton, W. D., Greisen, E. W., Yin, Q. F., Perley, R. A., Taylor, G. B., & Broderick, J. J. 1998, AJ, 115, 1693
 Conroy, M. A., Deponte, J., Moran, J. F., Orszak, J. S., Roberts, W. P., & Schmidt, D. 1993, in ASP Conf. Ser. 52: Astronomical Data Analysis Software and Systems II, ed. J. B. R. J. Hanisch, R. J. V. Brissenden, Vol. 2, 238
 Cooray, A. R., Grego, L., Holzappel, W. L., Joy, M., & Carlstrom, J. E. 1998, AJ, 115, 1388
 Crawford, C. S., Allen, S. W., Ebeling, H., Edge, A. C., & Fabian, A. C. 1999, MNRAS, 306, 857
 Crawford, C. S., Edge, A. C., Fabian, A. C., Allen, S. W., Böhringer, H., Ebeling, H., McMahon, R. G., & Voges, W. 1995, MNRAS, 274, 75
 Dawson, K. S., Holzappel, W. L., Carlstrom, J. E., Joy, M., LaRoque, S. J., & Reese, E. D. 2001, ApJ, 553, L1
 de Bernardis, P., et al. 2002, ApJ, 564, 559
 Dell'Antonio, I. P., Geller, M. J., & Fabricant, D. G. 1995, AJ, 110, 502
 Dennison, B. 1980, ApJ, 239, L93
 Dickey, J. M. & Lockman, F. J. 1990, ARA&A, 28, 215
 Dolag, K. & Ensslin, T. A. 2000, A&A, 362, 151
 Dolgov, A. D., Hansen, S. H., Pastor, S., & Semikoz, D. V. 2001, ApJ, 554, 74
 Donahue, M. 1996, ApJ, 468, 79
 Donahue, M., Voit, G. M., Scharf, C. A., Gioia, I. M., Mullis, C. R., Hughes, J. P., & Stocke, J. T. 1999, ApJ, 527, 525
 Dressler, A. & Gunn, J. E. 1992, ApJS, 78, 1

- Ebeling, H., Edge, A. C., Allen, S. W., Crawford, C. S., Fabian, A. C., & Huchra, J. P. 2000a, *MNRAS*, 318, 333
- Ebeling, H., Edge, A. C., Bohringer, H., Allen, S. W., Crawford, C. S., Fabian, A. C., Voges, W., & Huchra, J. P. 1998, *MNRAS*, 301, 881
- Ebeling, H., Edge, A. C., Fabian, A. C., Allen, S. W., Crawford, C. S., & Bohringer, H. 1997, *ApJ*, 479, L101
- Ebeling, H., Edge, A. C., & Henry, J. P. 2001, *ApJ*, 553, 668
- Ebeling, H., et al. 2000b, *ApJ*, 534, 133
- Ebeling, H., Voges, W., Bohringer, H., Edge, A. C., Huchra, J. P., & Briel, U. G. 1996a, *MNRAS*, 283, 1103
- . 1996b, *MNRAS*, 281, 799
- Elbaz, D., Arnaud, M., & Böhringer, H. 1995, *A&A*, 293, 337
- Ensslin, T. A., Biermann, P. L., Klein, U., & Kohle, S. 1998, *A&A*, 332, 395
- Fabian, A. C. 1994, *ARA&A*, 32, 277
- Fabian, A. C., Mushotzky, R. F., Nulsen, P. E. J., & Peterson, J. R. 2001, *MNRAS*, 321, L20
- Fairley, B. W., Jones, L. R., Scharf, C., Ebeling, H., Perlman, E., Horner, D., Wegner, G., & Malkan, M. 2000, *MNRAS*, 315, 669
- Fassnacht, C. D., Pearson, T. J., Readhead, A. C. S., Browne, I. W. A., Koopmans, L. V. E., Myers, S. T., & Wilkinson, P. N. 1999, *ApJ*, 527, 498
- Fixsen, D. J., Cheng, E. S., Gales, J. M., Mather, J. C., Shafer, R. A., & Wright, E. L. 1996, *ApJ*, 473, 576
- Freedman, W. L., et al. 2001, *ApJ*, 553, 47
- Geller, M. J. & Beers, T. C. 1982, *PASP*, 94, 421
- Gioia, I. M. & Luppino, G. A. 1994, *ApJS*, 94, 583
- Gioia, I. M., Maccacaro, T., Schild, R. E., Wolter, A., Stocke, J. T., Morris, S. L., & Henry, J. P. 1990, *ApJS*, 72, 567
- Giovannini, G. & Feretti, L. 2000, *New Astronomy*, 5, 335
- Giovannini, G., Tordi, M., & Feretti, L. 1999, *New Astronomy*, 4, 141
- Girardi, M., Fadda, D., Escalera, E., Giuricin, G., Mardirossian, F., & Mezzetti, M. 1997, *ApJ*, 490, 56
- Gómez, P. L., Hughes, J. P., & Birkinshaw, M. 2000, *ApJ*, 540, 726
- Goobar, A., et al. 2000, *Physica Scripta Volume T*, 85, 47
- Gould, R. J. 1980, *ApJ*, 238, 1026
- Grainge, K., Grainger, W. F., Jones, M. E., Kneissl, R., Pooley, G. G., & Saunders, R. 2002a, *MNRAS*, 329, 890
- Grainge, K., Jones, M., Pooley, G., Saunders, R., & Edge, A. 1993, *MNRAS*, 265, L57
- Grainge, K., Jones, M. E., Pooley, G., Saunders, R., Edge, A., & Kneissl, R. 2002b, *MNRAS*–submitted: astro-ph/9904165
- Grego, L., Carlstrom, J. E., Joy, M. K., Reese, E. D., Holder, G. P., Patel, S., Cooray, A. R., & Holzappel, W. L. 2000, *ApJ*, 539, 39
- Grego, L., Carlstrom, J. E., Reese, E. D., Holder, G. P., Holzappel, W. L., Joy, M. K., Mohr, J. J., & Patel, S. 2001, *ApJ*, 552, 2
- Hanisch, R. J. 1982, *A&A*, 116, 137
- Herbig, T., Lawrence, C. R., Readhead, A. C. S., & Gulkis, S. 1995, *ApJ*, 449, L5
- Herrnstein, J. R., et al. 1999, *Nature*, 400, 539
- Holder, G. P., Mohr, J. J., Carlstrom, J. E., Evrard, A. E., & Leitch, E. M. 2000, *ApJ*, 544, 629
- Holzappel, W. L., et al. Ade, P. A. R., Church, S. E., Mauskopf, P. D., Rephaeli, Y., Wilbanks, T. M., & Lange, A. E. 1997a, *ApJ*, 481, 35
- Holzappel, W. L., et al. 1997b, *ApJ*, 480, 449
- Holzappel, W. L., Carlstrom, J. E., Grego, L., Holder, G., Joy, M., & Reese, E. D. 2000, *ApJ*, 539, 57
- Hughes, J. P. & Birkinshaw, M. 1998, *ApJ*, 501, 1
- Inagaki, Y., Sugimoto, T., & Suto, Y. 1995, *PASJ*, 47, 411
- Itoh, N., Kohyama, Y., & Nozawa, S. 1998, *ApJ*, 502, 7
- Jaffe, W. 1980, *ApJ*, 241, 925
- Jaffe, W. J. 1977, *ApJ*, 212, 1
- Jones, L. R., Scharf, C., Ebeling, H., Perlman, E., Wegner, G., Malkan, M., & Horner, D. 1998, *ApJ*, 495, 100
- Jones, M., et al. 1993, *Nature*, 365, 320
- Jones, M. E., et al. 2002, *MNRAS*–submitted: astro-ph/0103046
- Kalloglyan, A. T., Nanni, D., & Vignato, A. 1990, *Astrophysics*, 31, 672
- Kempner, J. C. & Sarazin, C. L. 2001, *ApJ*, 548, 639
- Kendall, M. & Stuart, A. 1979, *The Advanced Theory of Statistics. Vol.2: Inference and Relationship* (London: Griffin, 1979, 4th ed.), 246
- Kneib, J. P., Mellier, Y., Fort, B., & Mathez, G. 1993, *A&A*, 273, 367
- Kneib, J. P., Mellier, Y., Pello, R., Miralda-Escude, J., Le Borgne, J., Bohringer, H., & Picat, J. 1995, *A&A*, 303, 27
- Kolb, E. W. & Turner, M. S. 1990, in *Frontiers in Physics*, Reading, MA: Addison-Wesley, 1988, 1990
- Komatsu, E., Kitayama, T., Suto, Y., Hattori, M., Kawabe, R., Matsuo, H., Schindler, S., & Yoshikawa, K. 1999, *ApJ*, 516, L1
- Lamarre, J. M., et al. 1998, *ApJ*, 507, L5
- Le Borgne, J. F., Pello, R., & Sanahuja, B. 1992, *A&AS*, 95, 87
- Liang, H., Hunstead, R. W., Birkinshaw, M., & Andreani, P. 2000, *ApJ*, 544, 686
- Lovell, J. E. J., Jauncey, D. L., Reynolds, J. E., Wieringa, M. H., King, E. A., Tzioumis, A. K., McCulloch, P. M., & Edwards, P. G. 1998, *ApJ*, 508, L51
- Maccacaro, T., Wolter, A., McLean, B., Gioia, I. M., Stocke, J. T., della Ceca, R., Burg, R., & Faccini, R. 1994, *Astrophys. Lett.*, 29, 267
- Majumdar, S. & Nath, B. B. 2000, *ApJ*, 542, 597
- Markevitch, M. 1997, *ApJ*, 483, L17
- Markevitch, M., Mushotzky, R., Inoue, H., Yamashita, K., Furuzawa, A., & Tawara, Y. 1996, *ApJ*, 456, 437
- Markevitch, M., et al. 2000, *ApJ*, 541, 542
- Mason, B. S. 1999, PhD thesis, University of Pennsylvania
- Mason, B. S., Myers, S. T., & Readhead, A. C. S. 2001, *ApJ*, 555, L11
- Mathiesen, B., Evrard, A. E., & Mohr, J. J. 1999, *ApJ*, 520, L21
- Mauskopf, P. D., et al. 2000, *ApJ*, 538, 505
- Mellier, Y., Soucail, G., Fort, B., & Mathez, G. 1988, *A&A*, 199, 13
- Moffet, A. T. & Birkinshaw, M. 1989, *AJ*, 98, 1148
- Mohr, J. J., Evrard, A. E., Fabricant, D. G., & Geller, M. J. 1995, *ApJ*, 447, 8
- Mohr, J. J., Mathiesen, B., & Evrard, A. E. 1999, *ApJ*, 517, 627
- Molnar, S. M. & Birkinshaw, M. 1999, *ApJ*, 523, 78
- Mushotzky, R. F. & Scharf, C. A. 1997, *ApJ*, 482, L13
- Myers, S. T., Baker, J. E., Readhead, A. C. S., Leitch, E. M., & Herbig, T. 1997, *ApJ*, 485, 1
- Nagai, D. & Mohr, J. J. 2002, *ApJ*–submitted
- Nagai, D., Sulkanen, M. E., & Evrard, A. E. 2000, *MNRAS*, 316, 120
- Nevalainen, J., Markevitch, M., & Forman, W. 2000, *ApJ*, 536, 73
- Ota, N., Mitsuda, K., & Fukazawa, Y. 1998, *ApJ*, 495, 170
- Patel, S. K., et al. 2000, *ApJ*, 541, 37
- Peacock, J. A. 1999, *Cosmological physics* (Cosmological physics. Publisher: Cambridge, UK: Cambridge University Press, 1999. ISBN: 0521422701)
- Pearson, T. J., Shepherd, M. C., Taylor, G. B., & Myers, S. T. 1994, *BAAS*, 185, 0808
- Peres, C. B., Fabian, A. C., Edge, A. C., Allen, S. W., Johnstone, R. M., & White, D. A. 1998, *MNRAS*, 298, 416
- Perlmutter, S., et al. 1999, *ApJ*, 517, 565
- Peterson, J. R., et al. 2001, *A&A*, 365, L104
- Pointecouteau, E., Giard, M., Benoit, A., Désert, F. X., Bernard, J. P., Coron, N., & Lamarre, J. M. 2001, *ApJ*, 552, 42
- Pointecouteau, E., Giard, M., Benoit, A., Désert, F. X., Aghanim, N., Coron, N., Lamarre, J. M., & Delabrouille, J. 1999, *ApJ*, 519, L115
- Pospieszalski, M. W., Lakatos, W. J., Nguyen, L. D., Lui, M., Liu, T., Le, M., Thompson, M. A., & Delaney, M. J. 1995, *IEEE MTT-S Int. Microwave Symp.*, 1121
- Pryke, C., Halverson, N. W., Leitch, E. M., Kovac, J., Carlstrom, J. E., Holzappel, W. L., & Dragovan, M. 2002, *ApJ*, 568, 46
- Raymond, J. C. & Smith, B. W. 1977, *ApJS*, 35, 419
- Reese, E. D., et al. 2000, *ApJ*, 533, 38
- Rephaeli, Y. 1995, *ApJ*, 445, 33
- Rephaeli, Y. & Yankovitch, D. 1997, *ApJ*, 481, L55
- Riess, A. G., et al. 1998, *AJ*, 116, 1009
- Roettiger, K., Stone, J. M., & Mushotzky, R. F. 1997, *ApJ*, 482, 588
- Roland, J. 1981, *A&A*, 93, 407
- Rudy, D. J. 1987, PhD thesis, California Inst. of Tech., Pasadena.
- Sault, R. J., Teuben, P. J., & Wright, M. C. H. 1995, *ASP Conf. Ser.* 77: *Astronomical Data Analysis Software and Systems IV*, 4, 433
- Saunders, R., et al. 1999, *MNRAS*–submitted: astro-ph/9904168
- Sazonov, S. Y. & Sunyaev, R. A. 1998a, *ApJ*, 508, 1
- . 1998b, *Astronomy Letters*, 24, 553
- Scharf, C. A., Jones, L. R., Ebeling, H., Perlman, E., Malkan, M., & Wegner, G. 1997, *ApJ*, 477, 79
- Schechter, P. L., et al. 1997, *ApJ*, 475, L85
- Schindler, S., et al. 1995, *A&A*, 299, L9
- Schindler, S., Hattori, M., Neumann, D. M., & Bohringer, H. 1997, *A&A*, 317, 646
- Schlickeiser, R., Sievers, A., & Thiemann, H. 1987, *A&A*, 182, 21
- Schmidt, B. P., et al. 1998, *ApJ*, 507, 46
- Scoville, N. Z., Carlstrom, J. E., Chandler, C. J., Phillips, J. A., Scott, S. L., Tilanus, R. P. J., & Wang, Z. 1993, *PASP*, 105, 1482
- Smail, I., Dressler, A., Kneib, J., Ellis, R. S., Couch, W. J., Sharples, R. M., & Oemler, A. J. 1996, *ApJ*, 469, 508
- Snowden, S. L. 1998, *ApJS*, 117, 233
- Snowden, S. L., McCammon, D., Burrows, D. N., & Mendenhall, J. A. 1994, *ApJ*, 424, 714
- Soucail, G., Mellier, Y., Fort, B., Mathez, G., & Cailloux, M. 1988, *A&A*, 191, L19
- Stebbins, A. 1997, preprint: astro-ph/9709065
- Stocke, J. T., Morris, S. L., Gioia, I. M., Maccacaro, T., Schild, R., Wolter, A., Fleming, T. A., & Henry, J. P. 1991, *ApJS*, 76, 813
- Stomp, R., et al. 2001, *ApJ*, 561, L7
- Struble, M. F. & Rood, H. J. 1991, *ApJS*, 77, 363

- . 1999, *ApJS*, 125, 35
Sulkanen, M. E. 1999, *ApJ*, 522, 59
Sunyaev, R. A. & Zel'dovich, Y. B. 1970, *Comments Astrophys. Space Phys.*, 2, 66
—. 1972, *Comments Astrophys. Space Phys.*, 4, 173
Tamura, T., et al. 2001, *A&A*, 365, L87
Tsuboi, M., Miyazaki, A., Kasuga, T., Matsuo, H., & Kuno, N. 1998, *PASJ*, 50, 169
Watkins, R. 1997, *MNRAS*, 292, L59
White, D. A. & Fabian, A. C. 1995, *MNRAS*, 273, 72
Worrall, D. M., et al. 1992, in *Data Analysis in Astronomy IV*, ed. V. Di Gesù et al. (New York: Plenum Press), 145